Revisiting the Activity Origin of $PtAu_{24}(SR)_{18}$ Nanocluster for Enhanced Electrocatalytic Hydrogen Evolution by Combining First-Principles Simulations with Experimental *in Situ* FTIR Technique

Fang Sun,[a,⊥] Lubing Qin,[b,⊥] Zhenghua Tang[b]* and Qing Tang[a]*

[a] F. Sun, Prof. Q. Tang

School of Chemistry and Chemical Engineering, Chongqing Key Laboratory of Chemical Theory and Mechanism, Chongqing University, Chongqing 401331, China.

E-mail: qingtang@cqu.edu.cn

[b] L. Qin, Prof. Z. Tang

New Energy Research Institute, School of Environment and Energy, South China University of Technology, Guangzhou Higher Education Mega Center, Guangzhou, 510006, China.

E-mail: zhht@scut.edu.cn

⊥ F.S. and L.Q. contributed equally to this work.

Supporting information for this article is given via a link at the end of the document.

Table of Contents

Computational methods and experimental section

Supporting Figures

Figure S11. AIMD snapshots of proton attack to Au in $PtAu_{24}(SCH_3)_{18}$ NC after the breaking of the first Au(surface)-S bond under U_{RHE} = -0.3 V.

Figure S12. Three representative sites of H bonding on dethiolated $PtAu_{24}(SCH_3)_{17}$ NC.

Figure S13. The relationships between the excess electrons and the corresponded electrode potential on dethiolated $PtAu_{24}(SCH_3)_{17}$ and the H* systems.

Figure S14. Calculated free energies (points) and polynomial fits (lines) of dethiolated $PtAu_{24}(SCH_3)_{17}$ and the H* systems as a function of potential.

Figure S15. Free energy changes of the each steps as a function of U_{RHE}.

Figure S16. Free energy changes of the HER reaction steps as a function of electrode potential U_{RHE} in pH = 3 on dethiolated $Au_{25}(SCH_3)_{17}$ NC.

Figure S17. The relationships between the excess electrons and the corresponded electrode potential on dethiolated $Au_{25}(SCH_3)_{17}$ and the H* systems.

Figure S18. The relationships between the excess electrons and the corresponded electrode potential on dethiolated $PtAu_{25}(SCH_3)_{17}$ with adsorption of two H.

Figure S19. The HER mechanism in dethiolated $PtAu_{25}(SCH_3)_{17}$; free energy changes as a function of U_{RHE}; free energy profile of the H_2 during the slow-growth simulation.

Figure S20. Dynamic evolution of bond length of Pt−H and Au−H for the H_2 formation via the Tafel process in dethiolated $PtAu_{25}(SCH_3)_{17}$.

Figure S21. PDOS of the s-states and d-states of the active Pt and Au-Au atoms in the intact $PtAu_{24}(SCH_3)_{18}$ and dethiolated $PtAu_{24}(SCH_3)_{17}$ NCs.

Figure S22. Free energy profiles of Heyrovsky reaction on S sites.

Figure S23. Free energy profiles of Heyrovsky reaction on Pt and dethiolated Au-Au.

Figure S24. LSV curves and Tafel plots of $Au_{24}Pt$ and Au_{25} before activation.

Figure S25. Remaining number of ligands in the $Au_{24}Pt$ cluster and the XPS spectra for Au 4f after 1 h electrochemical activation at different potentials in acid media (pH = 3).

Figure S26. The electrochemical impedance spectrum and the plots of current density as a function of scan rate derived from cyclic voltammograms of Au_{25} and $Au_{24}Pt$.

Figure S27. Electrochemical impedance spectra for $Au_{24}Pt$ and Au_{25} before and after

Supporting Tables

Computational methods and experimental section

1. First-principles computations

All first-principles calculations were carried out in Vienna ab initio simulation package code (VASP5.4.4),[1] and the projected-augmented wave (PAW) pseudopotential was adopted to describe the core electrons.[2] The electronic exchange-correlation potential was modelled using the Perdue-Burke-Ernzerhof (PBE) functional of the generalized gradient approximation (GGA),[3] and the Grimme's DFT + D3 method was employed to accurately describe the van der Waals interactions.[4] The plane-wave kinetic energy cutoff was set as 400 eV in the relaxation, while 350 eV was used in the AIMD simulations. The Γ point only was utilized to sample the Brillouin zone. The residual energy and forces of structure optimization were converged below 10^{-5} eV per atom and smaller than 0.02 eV/Å, respectively. Bader charges were obtained using the code developed by Henkelman group.[5]

2. Constant-potential hybrid-solvent model

The constant-potential hybrid-solvent model was used to determine the thermodynamic and kinetic energetics of reactions at the catalyst/solvent interface. The box size was set to be 18 × 18 × 28 $Å^3$, where 78 H_2O molecules were added along the z-axis to the local surface of $PtAu_{24}$ NC for thermodynamic calculation, and 78 H_2O molecules plus one H_3O^+ were constructed for kinetic simulation in acidic environments. The structure was pre-relaxed for 5 ps to ensure the stability of the hydrogen bond network. The so-called hybrid-solvent environment means that both the explicit water molecules and Poisson-Boltzmann implicit solvation model are considered in our simulation. Explicit models can detect the interactions between intermediates and surrounding water molecules. The implicit model can relate the system charge and electrode potential based on the fact that the electrostatic potential goes to zero in the electrolyte region, as implemented in the VASPsol.[6, 7] For an electrochemical system, the electrostatic potential can be analogous to the work function. Therefore, excess electrons can be introduced and subsequently calculated the work function (Φ) of each model to match the electrode potential according to U_{RHE} =

*(Φ - μ_{SHE})/e + 0.0592*pH*,[8] where Φ can be reflected by the Fermi level with respect to the electrostatic potential in the electrolyte region. μ_{SHE} is the absolute potential of the standard hydrogen electrode (SHE), which has been predicted to be 4.6 V from the VASPsol simulation.[9] In this work, the pH value was taken as 3, similar to the experimental HER measurements in a near acidic electrolyte environment.

3. Thermodynamic calculation

Based on the above model, different additional electrons can be introduced into the system to determine an electrochemical potential, labeled as the constant potential method (CPM). The Gibbs free energy can be calculated by[10, 11]

$$G = E_{DFT} + ZPE - TS - \mu_e \times N_e$$

Where E_{DFT} and *ZPE* are the DFT energy from the CPM, the difference of zero-point energy, and *T* and *S* are the temperature and entropy, respectively. *ZPE* and *S* are calculated by treating the adsorbate only as a vibration. μ_e is the electron energy, and can be calculated as $\mu_e = \mu_{SHE} - lel*U_{SHE}$. U_{SHE} is the applied potential versus SHE, and can be obtained through $U_{SHE} = U_{RHE} - 0.0592*pH$. N_e is the number of added electrons relative to the total electrons in the neutral system. The total free energy of each species were then fit to a quadratic function to obtain a continuous relationship between *G* and U_{RHE}, in the form[12]

$$G(U_{RHE}) = -\frac{1}{2}C(U_{RHE} - U_0)^2 + E_0$$

where U_0 is the potential of zero charge (PZC), E_0 is the corresponding free energy, and *C* is the capacitance of the surface. With these potential-energy curves, the *G* of each system for a specific U_{RHE} can be obtained, thereby determining the corresponding free energy changes (ΔG) of the two-step reduction in HER. For Volmer step (* + H^+ + e^- = H*), ΔG_1 of H adsorption is calculated as follows:[13]

$$\Delta G_1 = G_{sol}(H^{*Q2}) - G_{sol}(^{*Q1}) - G(H_2(g))/2 + |e|U_{RHE} + (Q2 - Q1)\mu_e$$

where *Q1* and *Q2* are the net charges on the $PtAu_{24}$ before and after H adsorption, which can be determined via the relationship between excess electrons (Q) and the corresponding U_{RHE}. For Heyrovsky step (H* + H^+ + e^- = H_2 + *), ΔG_2 can be derived as

$$\Delta G_2 = -\Delta G_1 + 2|e|U_{RHE}$$

For Tafel step on the same cluster surface (*2H = H_2 + *), $\Delta G_2'$ can be derived as

$$\Delta G_2' = G_{sol}(^{*Q1}) + G(H_2(g)) - G_{sol}\left(* \ 2H^{Q2'}\right) + (Q1 - Q2')\mu_e$$

4. Kinetic calculation

Before performing AIMD operations, each system was pre-optimized. All AIMD simulations were sampled in the NVT ensemble, and the Nose-Hoover thermostat is applied to keep the target temperature constant at 300 K with a time step of 1 fs. [14-18] Only the gamma-centered k-mesh was adopted in AIMD simulations. Considering the fluctuation of the work function, at least 8 snapshots were extracted from the AIMD trajectories to determine a corresponding average potential. To calculate the kinetic barriers, the "slow-growth" approach[19] was employed as implemented in VASP to obtain the free energy profile. In this method, the free energy
difference between the initial state (IS) and the final state (FS) is obtained by applying a holonomic constraint on the reaction coordinate (ξ) during MD simulations and integrating over the average unbiased force associated with the reaction coordinate:

$$w_{\xi IS-\xi FS} = \int_{\xi FS}^{\xi IS} d\xi \frac{dw}{d\xi} = \int_{\xi FS}^{\xi IS} d\xi \left\langle \frac{\partial H}{\partial \xi} \right\rangle_{\xi}$$

where the free energy gradient $\frac{dw}{d\xi}$ can be computed from the ensemble averaged derivative of Hamiltonian (H) over the variable ξ. For the solvated proton (H_3O^+) adsorption on the reaction sites (M) under acidic condition (* + H_3O^+ + e^- = H* + H_2O), the collective variable (CV) is defined by $CV = \xi(r) = d1\text{-}d2 = lr_M - r_Hl - lr_O - r_Hl$, where r_M refers to the coordinate of the reaction site, r_O refers to the coordinate of the O atom on H_3O^+, and r_H refers to the coordinate of the solvated proton on H_3O^+. For H_2 formation (H* + H_3O^+ + e^- = H_2 + * + H_2O), the CV is defined by $CV = \xi(r) = d1\text{-}d2 = lr_H - r_H'l - lr_O' - r_H'l$, where r_O' refers to the coordinate of the O atom on another H_3O^+, and r_H' refers to the coordinate of the solvated proton on another H_3O^+.

5. Materials

Methanol, ethanol, dichloromethane, ethyl acetate, *n*-hexane, tetrahydrofuran(THF), chloroauric acid trihydrate ($HAuCl_4.3H_2O$), triphenylphosphine

(PPh_3), 2-phenylethanethiol (Ph-CH_2CH_2SH), (Triphenylphosphine)gold(I) chloride (PPh_3AuCl) , sodium borohydride ($NaBH_4$), carbon black XC-72, commercial Pt/C catalyst, tetrakis (triphenylphosphine) platinu ($Pt(PPh_3)_4$) were all purchased from Energy Chemical (Shanghai, China). Ether and hydrochloric acid were bought from Guangzhou Dongzheng Chemical Reagent, China. Water was supplied using the Barnstead Nanopure water system with a resistivity of 18.3 MΩ cm^{-1}. All chemicals were used as received without further treatment.

6. Instruments

UV-visible absorbance spectra were recorded using a Shimadzu UV-1800 spectrometer. The electrospray ionization mass spectra (ESI-MS) of the nanoclusters (NCs) were acquired on a Bruker UItiMate3000 time-of-flight (TOF) system. ESI-MS instrumental parameters were maintained with the following values: Capillary voltage: -3.5 kV; dry temp.: 200 °C; nebulizer: 0.6 bar; dry gas: 6.01 mL min^{-1}. The electrochemical performance of the catalyst was evaluated on a CHI 630e electrochemical workstation. The *in suit* FTIR (ATR-SEIRAS) spectra was recorded using a Thermo Scientific 6300 spectrometer.

7. Preparation of the $Au_{24}Pt$ nanoclusters

$Au_{24}Pt$ was synthesized according to the method reported previously.[20] Firstly, 100 mL anhydrous ethanol and 2.5 g $Pt(PPh_3)_4$ were added into a 250 mL three-mouth flask successively, and then the mixture was heated and boiled under N_2 condition for 2 h. After that, the solution was filtered while hot to obtain yellow precipitate. The precipitate was washed with 30 mL cold ethanol. Finally, the yellow powder ($Pt(PPh_3)_3$) was obtained by vacuum drying. In addition, white acicular $Au(PPh_3)NO_3$ crystals were synthesized by the above reported literature.

$(PPh_3)AuNO_3$ was prepared by the following procedure. Typically, 2 g $(PPh_3)AuCl$ was dissolved in 40 mL of dichloromethane to prepare Solution A. Then, 1.37 g silver nitrate was dissolved in 125 mL of methanol to prepare Solution B. Subsequently, Solution A was dropwise added into Solution B and then the mixture was kept vigorous stirring for 1 h at room temperature. After filtration to remove the precipitates (AgCl), the supernatant was subjected to rotary evaporation to remove all

solvents, yielding a pale yellow solid. This solid was dissolved in 15 mL of dichloromethane and centrifuged to remove insoluble materials to obtain Solution C. Next, 60 mL of ethanol was added to Solution C and continuously pass N_2 gas through the system for 2 h, during which a large amount of white needle-like crystals precipitated out. The precipitates were filtered and washed with a large amount of ethanol to obtain $(PPh_3)AuNO_3$.

Next, 50 mL THF, 318 mg $Pt(PPh_3)_3$, 1 g $Au(PPh_3)NO_3$ were added into a 150 mL flask under the Ar gas atmosphere. Then, the system as a whole was sealed and mixed for 1 h, and hydrogen gas was injected into the system until the solution changes from light yellow to red and eventually produces a large amount of brown-red solid. The solid was obtained by centrifugation and washed with 10 mL THF, then the solid was dissolved in 10 mL methanol. 80 mL ether was slowly poured into the methanol liquid surface, and after standing for 48 h, a large number of brown-yellow needle-like crystals were precipitated on the bottle wall of the flask ($[Au_8Pt(PPh_3)_8](NO_3)_2$).

Finally, a 15 mL flask was charged with $AuClSMe_2$ (210 mg) and subsequently with THF (4 mL), and a transparent solution was formed after stirring. Soon after the formation of the suspension, PET (75 μL) in 2 mL THF was added dropwise to the well stirred suspension, resulting in a pale-yellow homogeneous solution (Solution A). EtOH (1 mL) was then added into a 50 mL tube charged with $[Au_8Pt(PPh_3)_8](NO_3)_2$ (120 mg), forming a dark red solution after stirring. The whole tube was subsequently cooled in a mixture of ice water at 0 ^oC for 30 mins. The solution was then diluted with THF (10 mL) and an ethanolic solution of $NaBH_4$ (0.10 M, 300 μL) was added, resulting in a fast coloration from dark red to black (Solution B). After 2 mins, solution A was added dropwise into Solution B over 12 mins. The color of the mixed solution gradually changed into yellowish-green. After stirring for 60 mins, NEt_3 (100 μL) was then added into the mixture, and the stirring was continued for an additional 1 h at 0 ^oC. After the addition of MeOH, the mixed solution was evaporated into dryness. The blackish-green residue was washed twice with EtOH (15 mL), and the residue was extracted using DCM (10 mL). The extract was evaporated, and the crude product was purified using column chromatography (Al_2O_3 beads; DCM: n-hexane = 5:4). The yale-

green band was collected and dried in vacuo, giving the $Au_{24}Pt(PET)_{18}$ product as dark green powder.

The synthetic route for $Au_{25}(PET)_{18}$ is basically the same as that for $Au_{24}Pt(PET)_{18}$, with the exception of replacing the precursor $[Au_8Pt(PPh_3)_8](NO_3)_2$ with $[Au_9(PPh_3)_8](NO_3)$ (the synthesis method for $[Au_9(PPh_3)_8](NO_3)$ is identical to that of $[Au_8Pt(PPh_3)_8](NO_3)_2$ without the addition of $Pt(PPh_3)_3$ at the beginning). Additionally, the purification of the product can be achieved by sequentially washing the crude product with a large amount of *n*-hexane (50 mL), ethanol (50 mL), and methanol (70 mL) several times.

8. Preparation of the catalyst ink

In a typical procedure, 10 mg of the $Au_{24}Pt$ or Au_{25} clusters and 5 mg of XC-72 were co-dissolved in 10 mL DCM, and the mixture was kept stirring for 2 h at room temperature. Then, vacuum distillation was used to remove the solvent to obtain some dry solid. The solid was then added into 1 mL ethanol and subjected to ultrasonic dispersion for a few mins to prepare the catalyst ink.

9. Electrochemical Measurements

The HER electrochemical measurements were performed using a conventional three-electrode system on an electrochemical workstation (CHI 630 e) in 0.5 M Na_2SO_4 (add HCl into the solution to adjust the pH of the system to be ~3), with a graphite rod (3 cm in diameter) as the counter electrode, an Ag/AgCl electrode as the reference electrode, and the glass carbon electrode (acreage 0.125 cm^2) as the working electrode. Then, 10 μL of the catalyst ink was added dropwise onto the glassy carbon electrode and dried naturally. Next, 10 μL of an ethanol solution containing 5% Nafion was dropped onto the glassy carbon electrode. The working electrode is completely prepared after the ethanol was evaporated. The linear sweep voltammetry (LSV) measurements were conducted in a potential range from 0.1 V to -0.5 V (vs. RHE) with a scan rate of 5 mVs^{-1}. The measured potentials were transformed into the reversible hydrogen electrode (RHE) scale using the following formula: $E_{RHE} = E_{Ag/AgCl} + 0.0591*pH + 0.197$.

The *in situ* infrared test (ATR-SEIRAS) method is similar to the electrochemical analysis method. The electrolyte with the same composition and concentration was first added into the *in situ* electrolytic cell, then the electrode with the catalyst ink was inserted, and the measurement was performed in the LSV way.

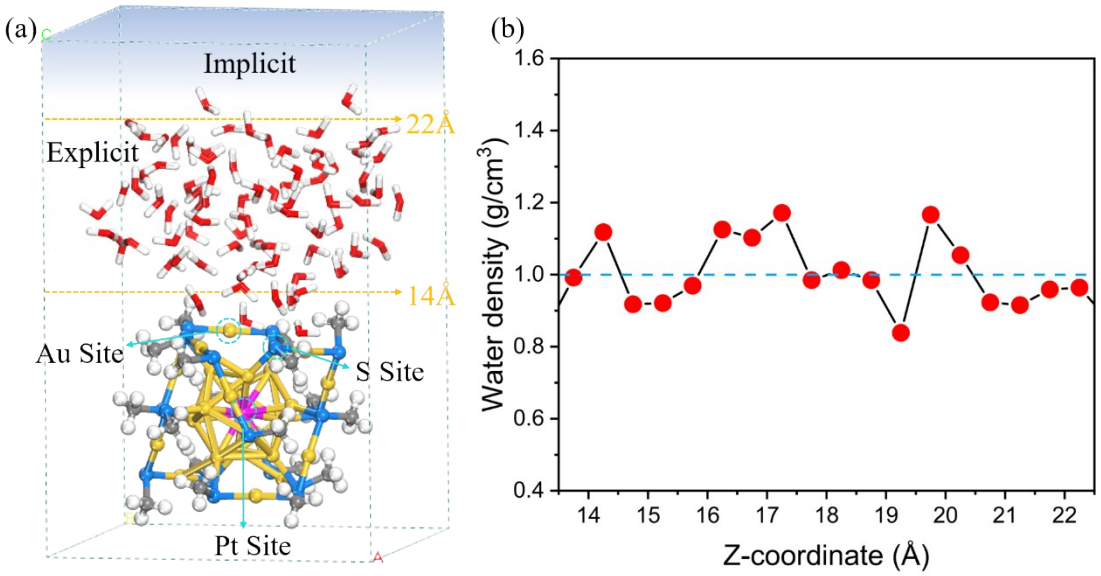

Figure S1. (a) The theoretical model of $PtAu_{24}(SCH_3)_{18}$ catalyst with hybrid-solvent environment (explicit + implicit) at potential of zero charge (PZC). The blue area above the water layer denotes an implicit solvation model. (b) Water density along the z-axis of the water adsorption layers (~ 14 to 22 Å) on $PtAu_{24}(SCH_3)_{18}$ NC during the structural relaxations. The 1-D density profiles of water were plotted by using the "Density Profile Tool" plugin implemented in VMD software. Color codes: yellow, Au; purple, Pt; blue, S; grey, C; red, O; white, H. The same color scheme is used in the figures below.

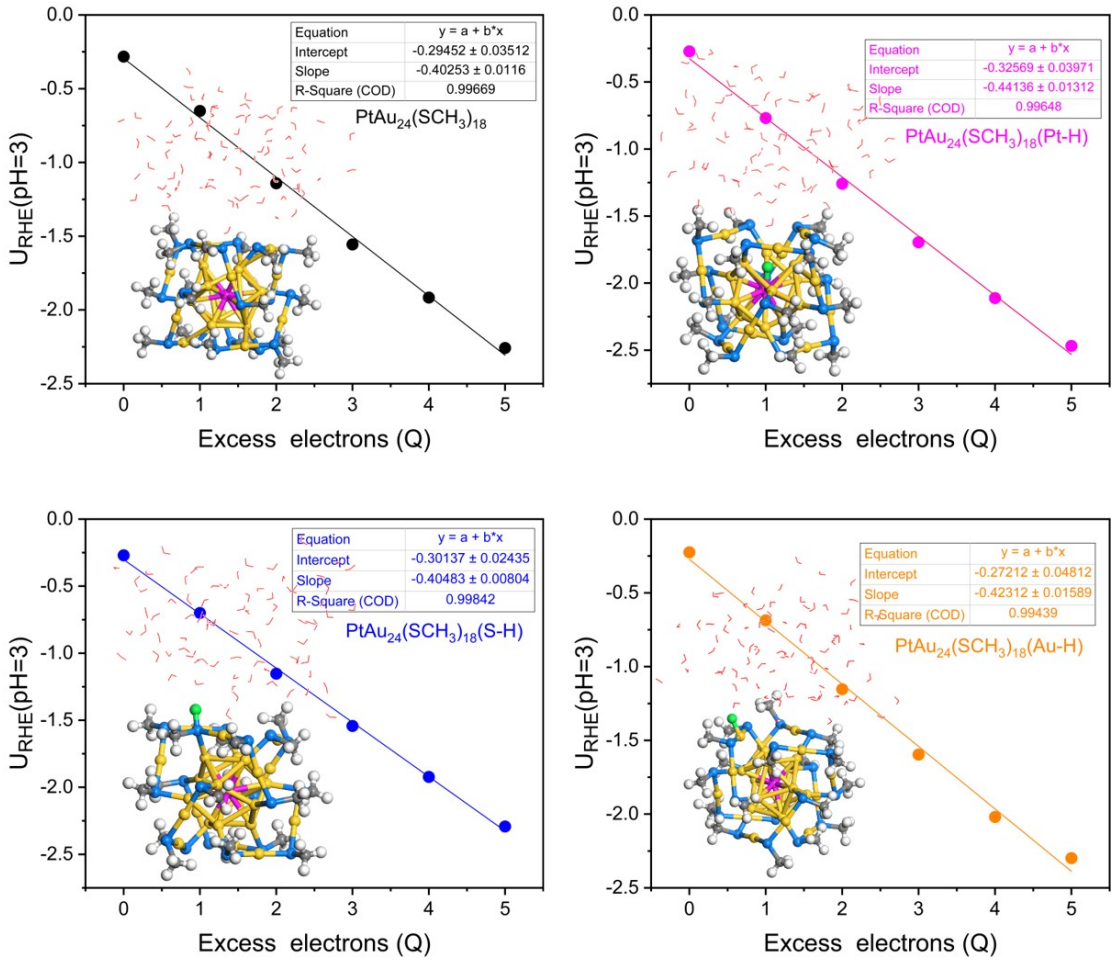

Figure S2. The relationships between the excess electrons (Q) and the corresponded electrode potential U_{RHE} in pH = 3 on intact $PtAu_{24}(SCH_3)_{18}$ and the H* system at its three different adsorption sites. The corresponding snapshots optimized using an excess electron of 5e can also be seen in the inset where the adsorbed H atom is highlighted in green. The same color scheme is used in the figures below.

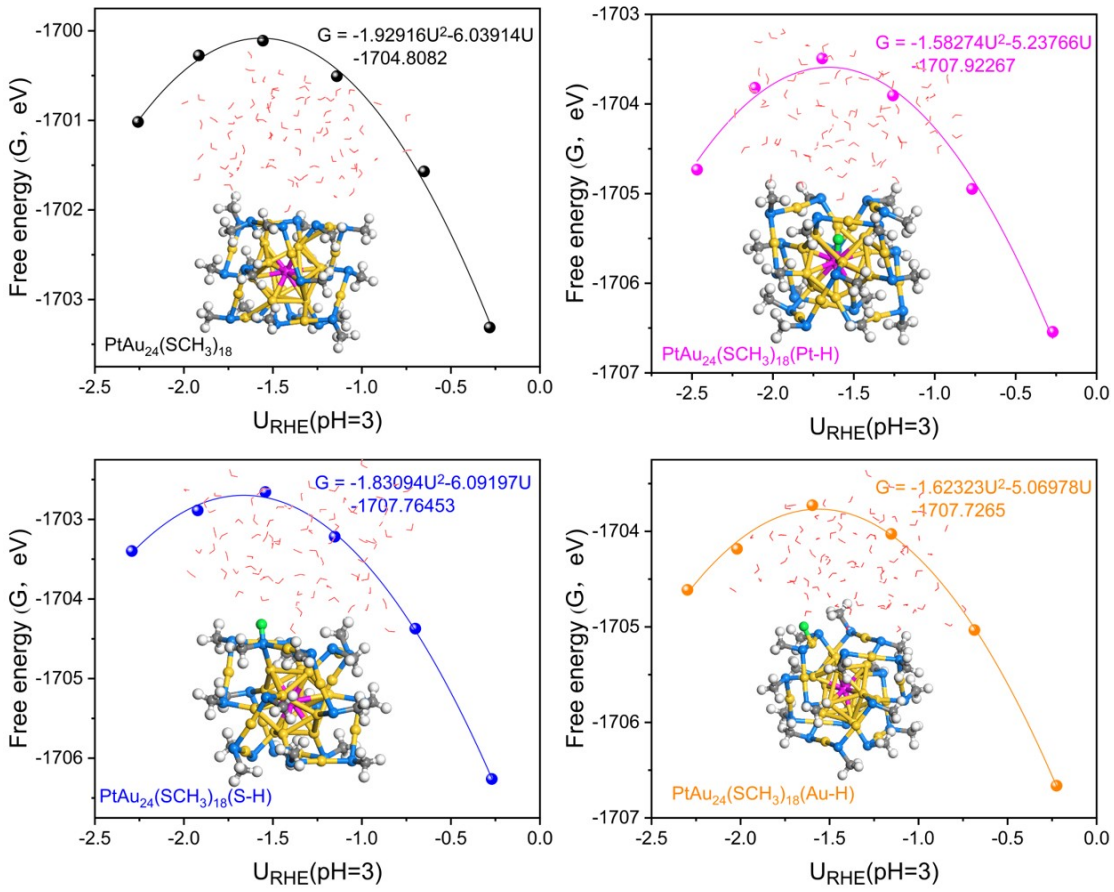

Figure S3. Calculated free energies (points) and polynomial fits (lines) of intact $PtAu_{24}(SCH_3)_{18}$ and the H* adsorbed system at three different sites as a function of potential U_{RHE} in pH = 3, calculated using the constant potential method (cpm). The corresponding geometric snapshots optimized using an excess electron of 5e can also be seen in the inset where the adsorbed H atom is highlighted in green.

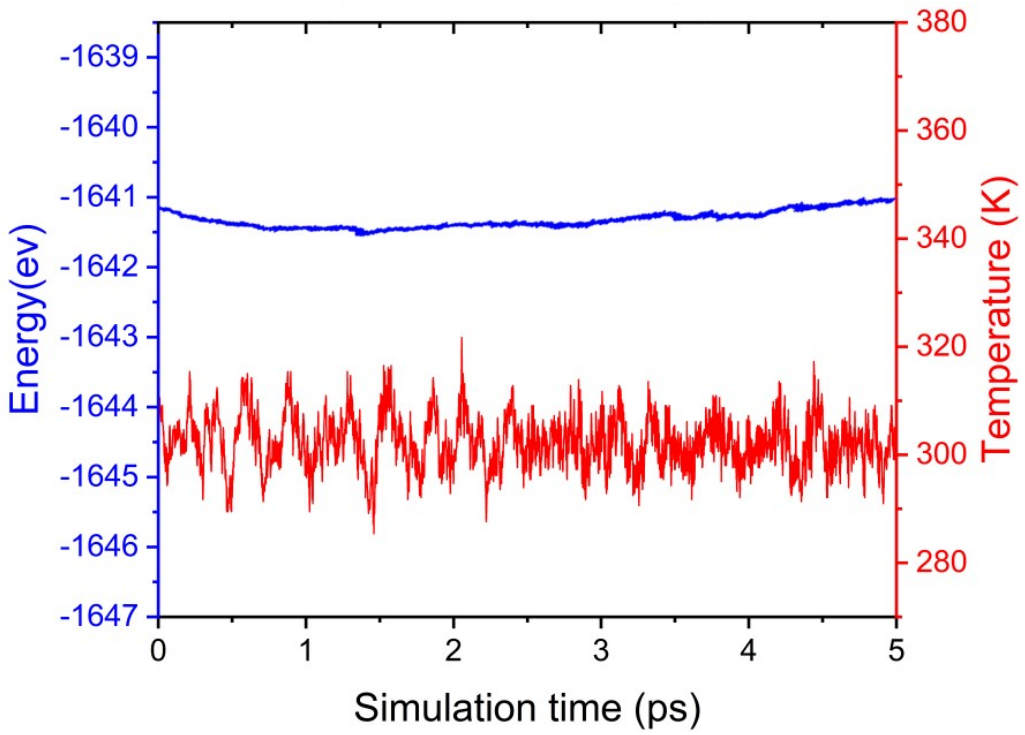

Figure S4. The energies and temperatures of 5 ps trajectory during the AIMD simulation of $PtAu_{24}(SCH_3)_{18}$ with 78 explicit water molecules.

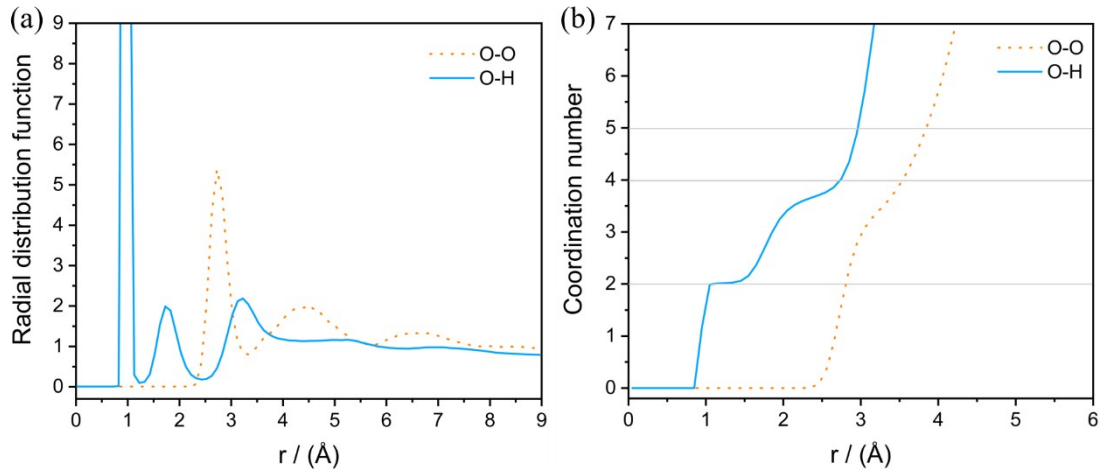

Figure S5. (a) Radial distribution function (RDF) and (b) integrated coordination number of O-O and O-H pairs of water from a 5 ps AIMD trajectory in our system.

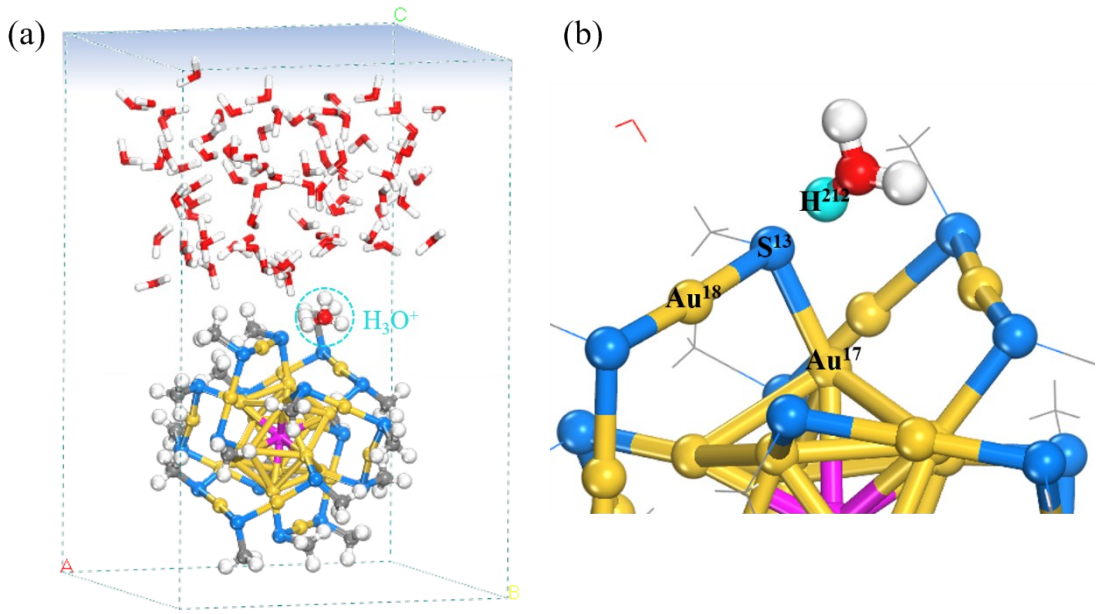

Figure S6. The theoretical model of (a) acid system at potential of zero charge (PZC) condition. The blue area above the water layer denotes an implicit solvation model. And (b) corresponds to the locally magnified image with some atomic markings. Possible transferred H^{212} atom from H_3O^+ to S atom is highlighted in turquoise, and the same color scheme is used in the figures below.

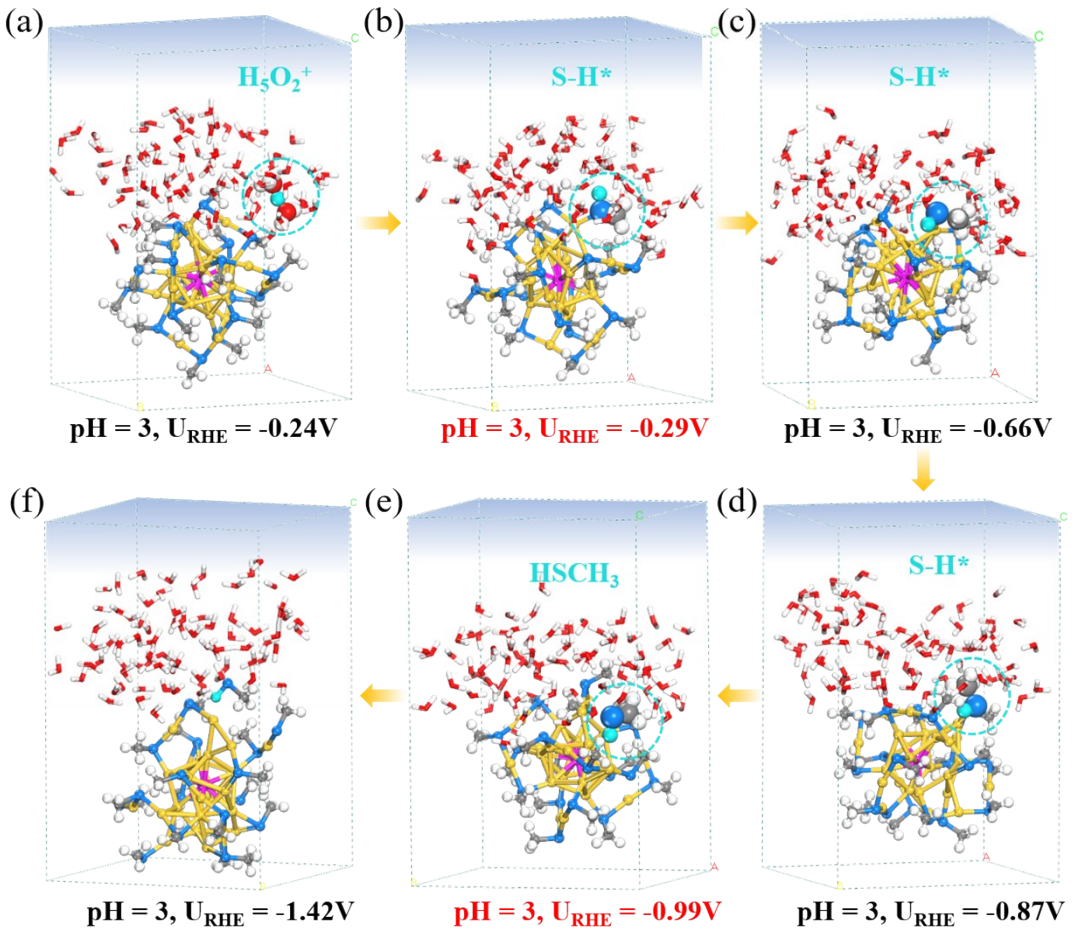

Figure S7. The corresponding equilibrated AIMD snapshot under different potential.

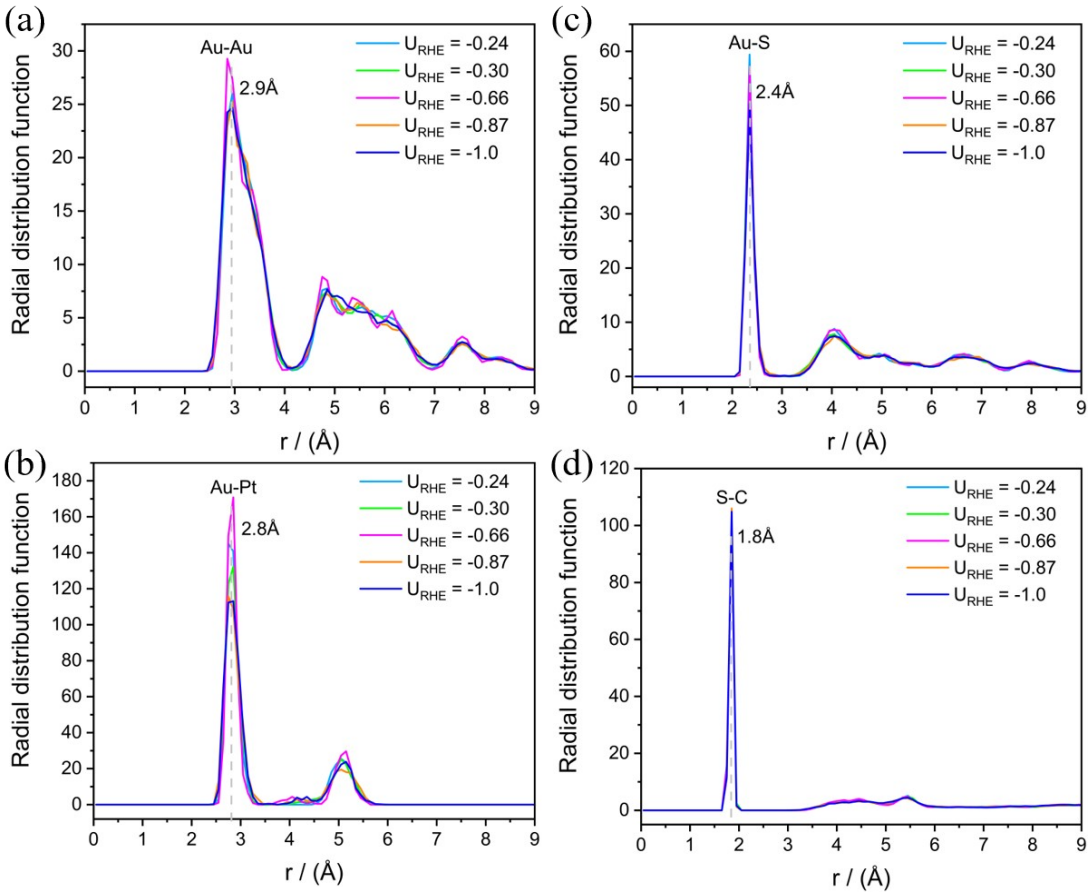

Figure S8. Radial distribution function (RDF) of Au-Au, Au-S, Au-Pt and S-C bonds from different constant potential AIMD trajectory.

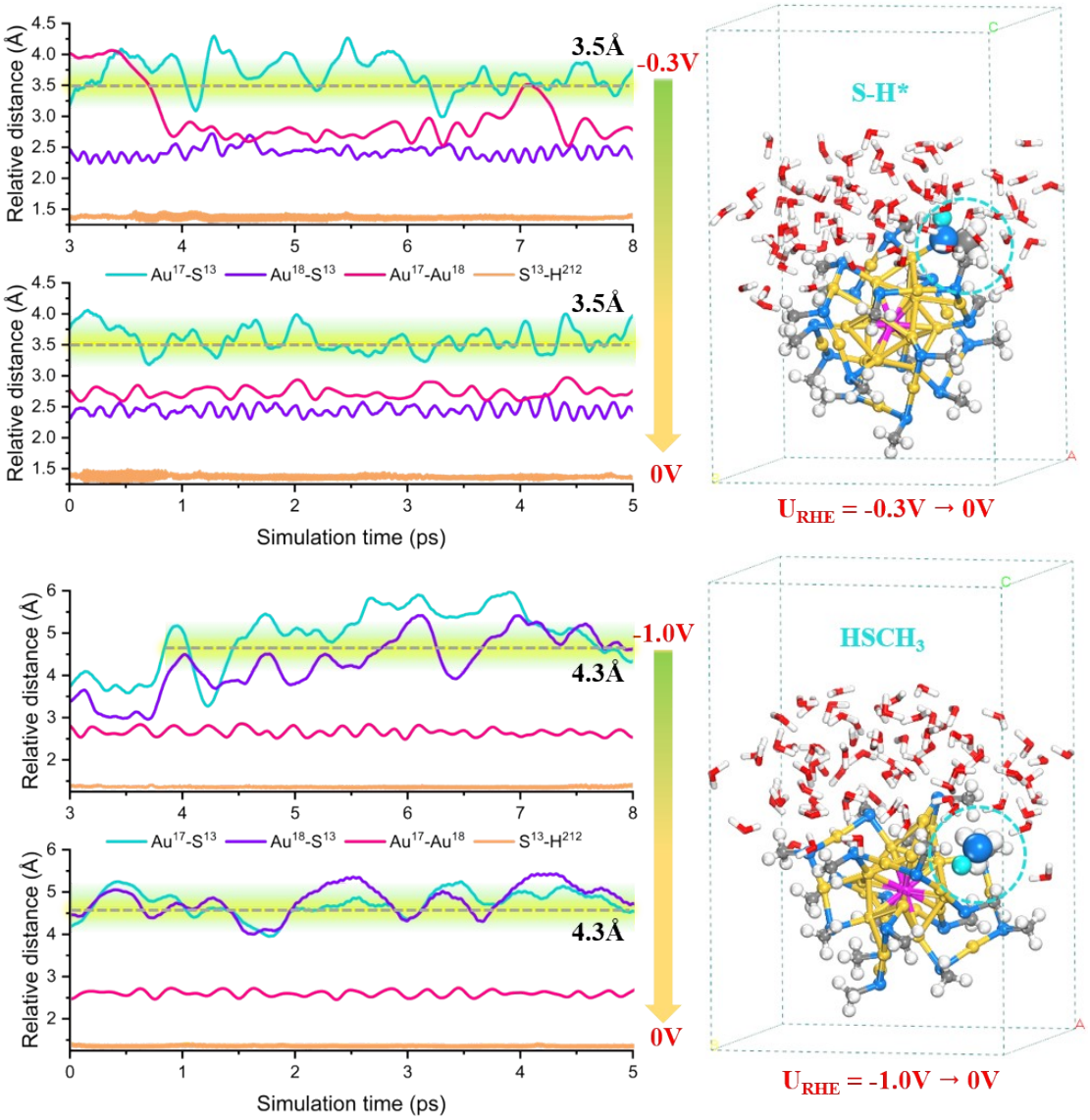

Figure S9. Comparison of the relative distances between representative atoms in equilibrium AIMD simulations after converting the potential to 0V vs RHE. The corresponding AIMD snapshot is shown on the right.

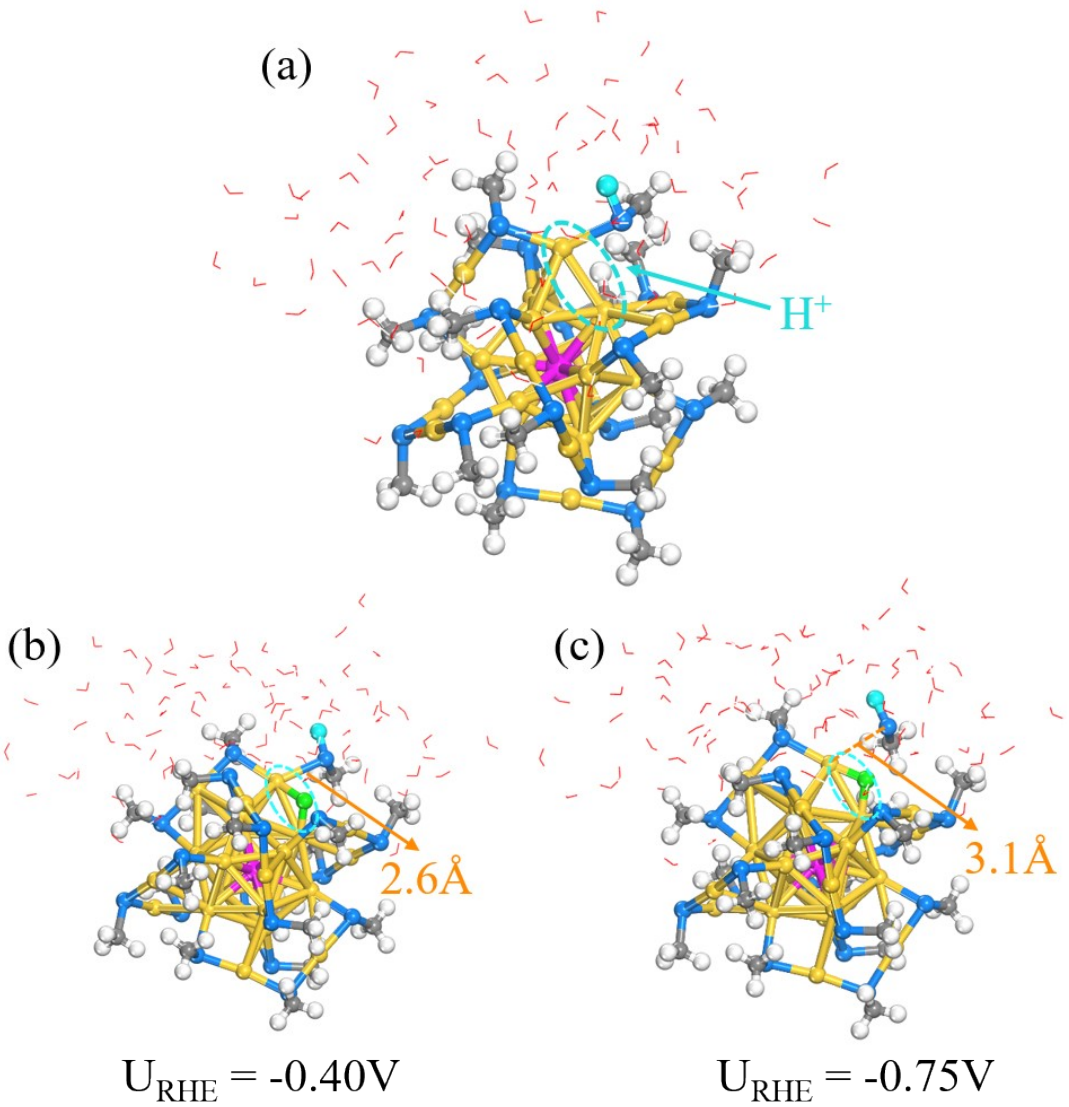

Figure S10. (a) Schematic illustration for the proton attack to the exposed bridging Au sites. (b) and (c) Views of the atomic structures of H* adsorbed to Au in $PtAu_{24}(SCH_3)_{18}$ NC after the breaking of the first Au(surface)-S bond at different potentials.

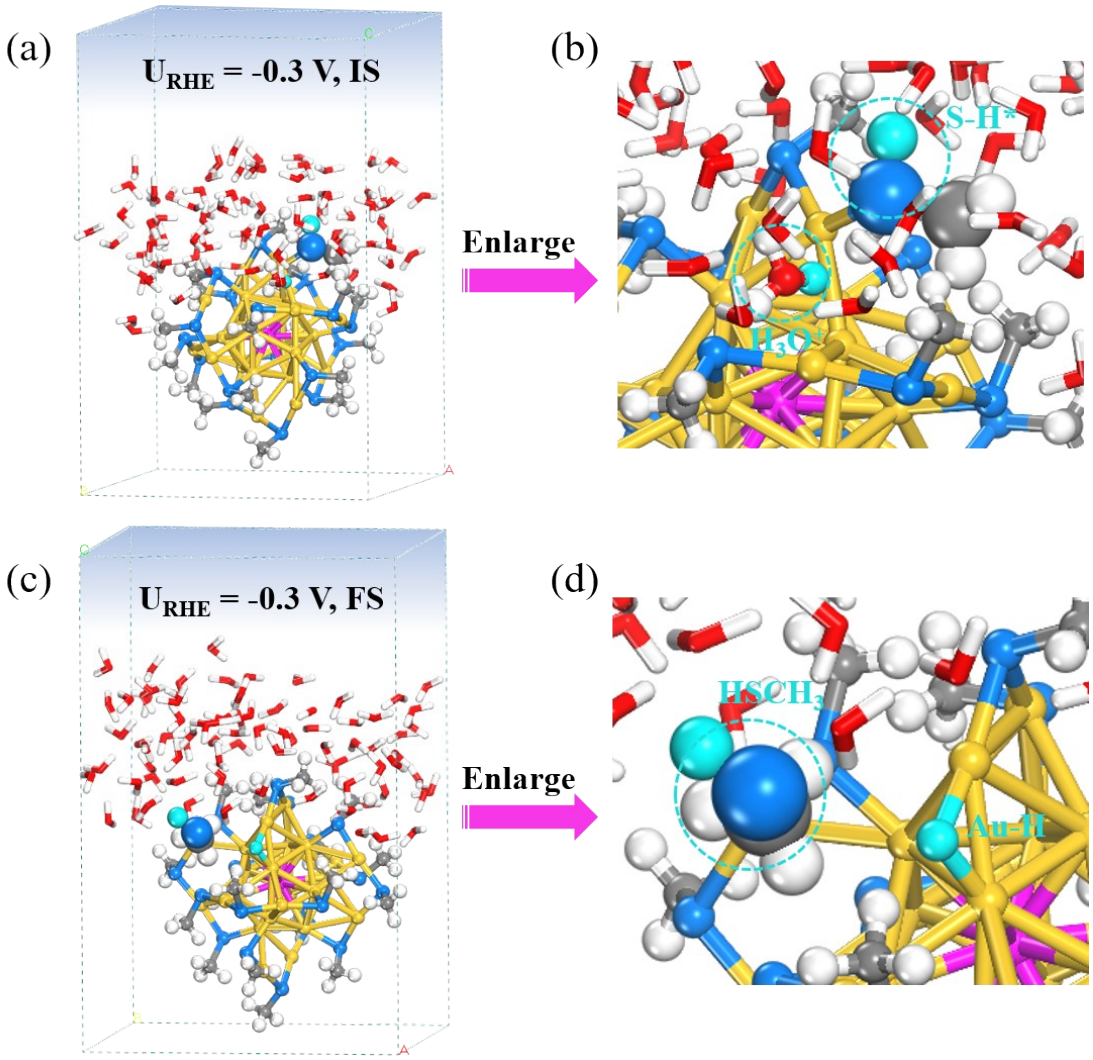

Figure S11. The initial (a) and final (c) AIMD snapshots of proton attack to Au in $PtAu_{24}(SCH_3)_{18}$ NC after the breaking of the first Au(surface)-S bond under U_{RHE} = -0.3 V. The blue area above the water layer denotes an implicit solvation model. (b) and (d) are the corresponding locally magnified images.

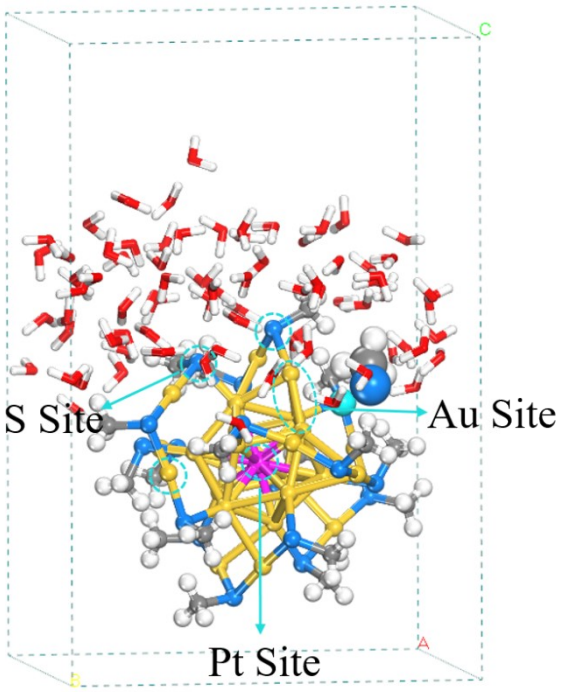

Figure S12. (a) Three representative sites of H bonding on dethiolated $PtAu_{24}(SCH_3)_{17}$ NC.

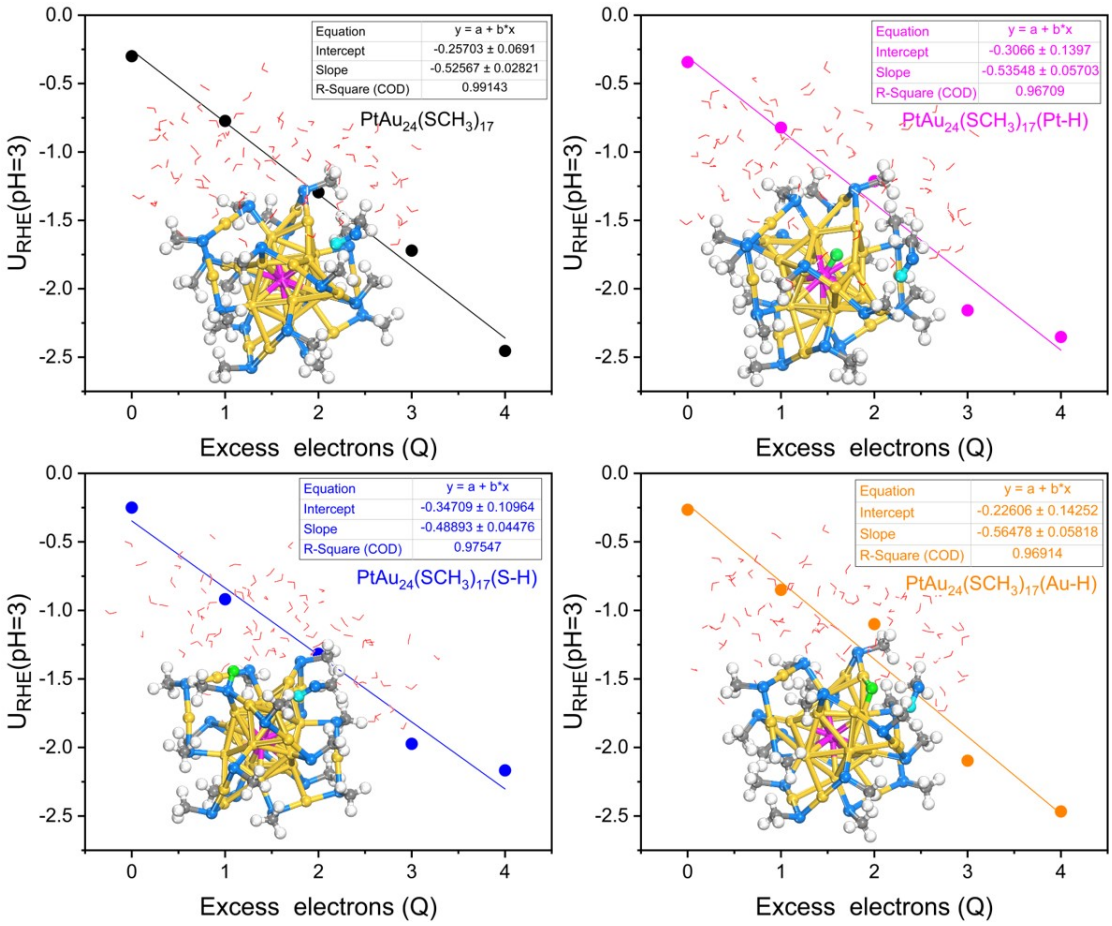

Figure S13. The relationships between the excess electrons (Q) and the corresponded electrode potential U_{RHE} in pH = 3 on dethiolated $PtAu_{24}(SCH_3)_{17}$ and the H* system at three different sites. The corresponding geometric snapshots optimized using an excess electron of 4e can also be seen in the inset where the adsorbed H* is highlighted in green.

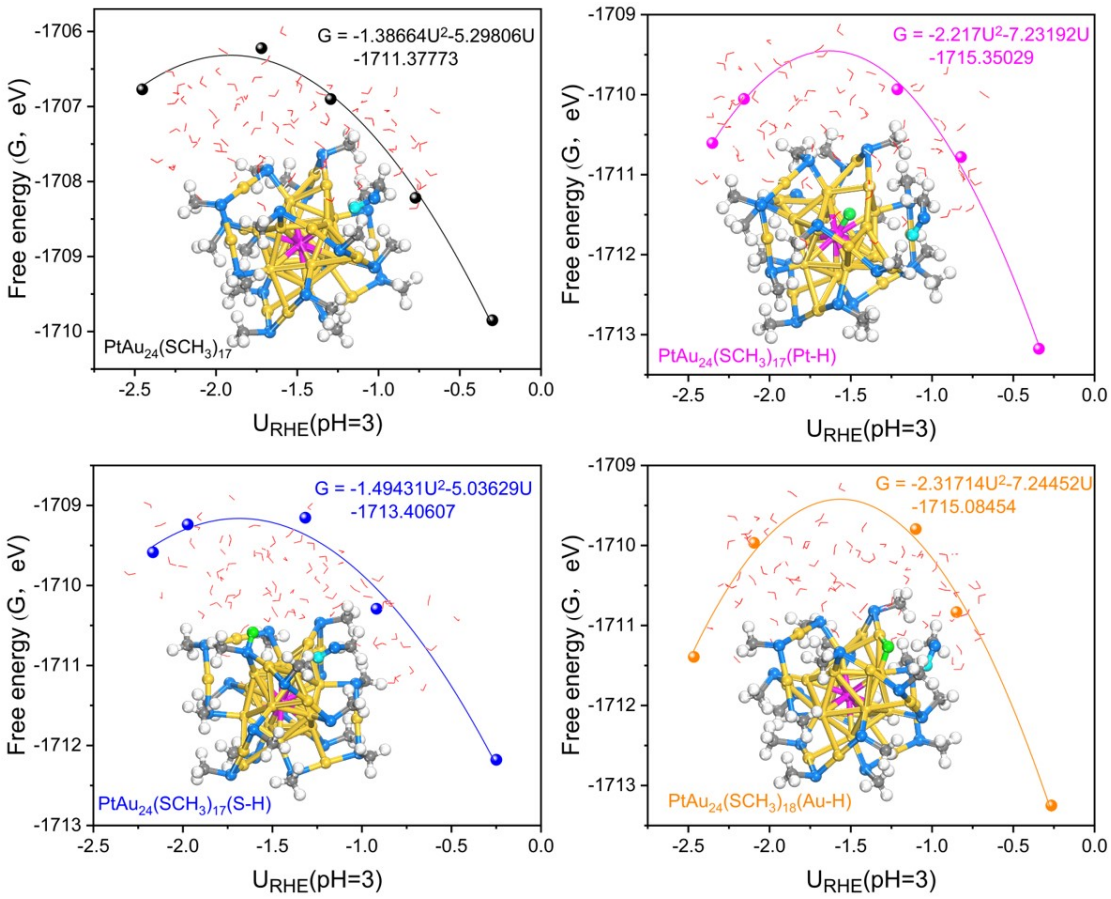

Figure S14. Calculated free energies (points) and polynomial fits (lines) of dethiolated $PtAu_{24}(SCH_3)_{17}$ and the H* system at its three different sites as a function of potential U_{RHE} in pH = 3, calculated using the constant potential method (cpm). The corresponding geometric snapshots optimized using an excess electron of 4e can also be seen in the inset where the adsorbed H* is highlighted in green.

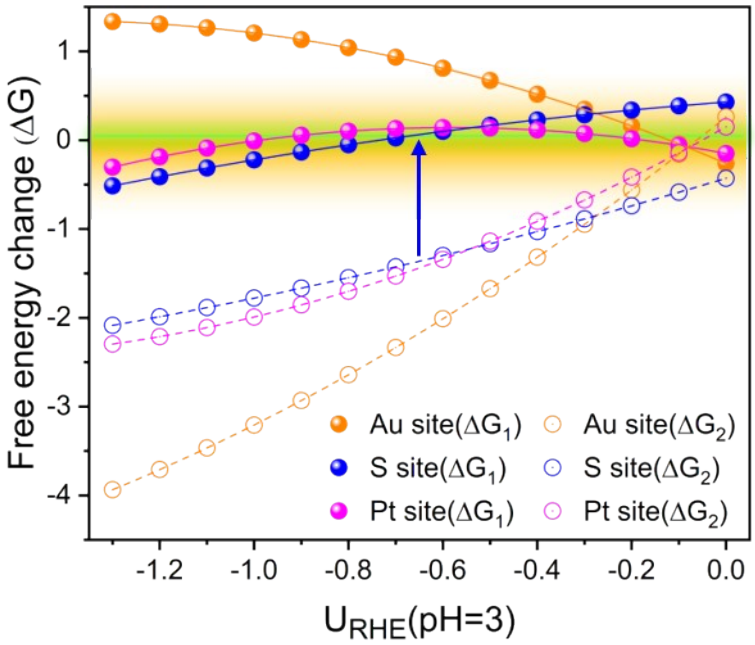

Figure S15. Free energy changes (ΔG) of the HER reaction steps as a function of electrode potential U_{RHE} in pH = 3.

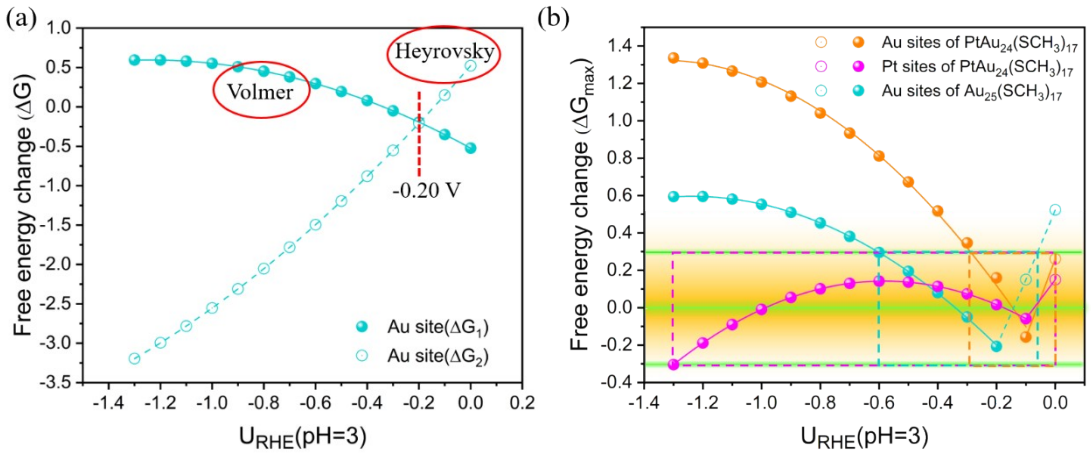

Figure S16. (a) Free energy changes (ΔG) of the HER reaction steps as a function of electrode potential U_{RHE} in pH = 3 on dethiolated $Au_{25}(SCH_3)_{17}$ NC. (b) Free energy changes of the PDS (ΔG_{max}) as a function of the electrode potential U_{RHE} in pH = 3.

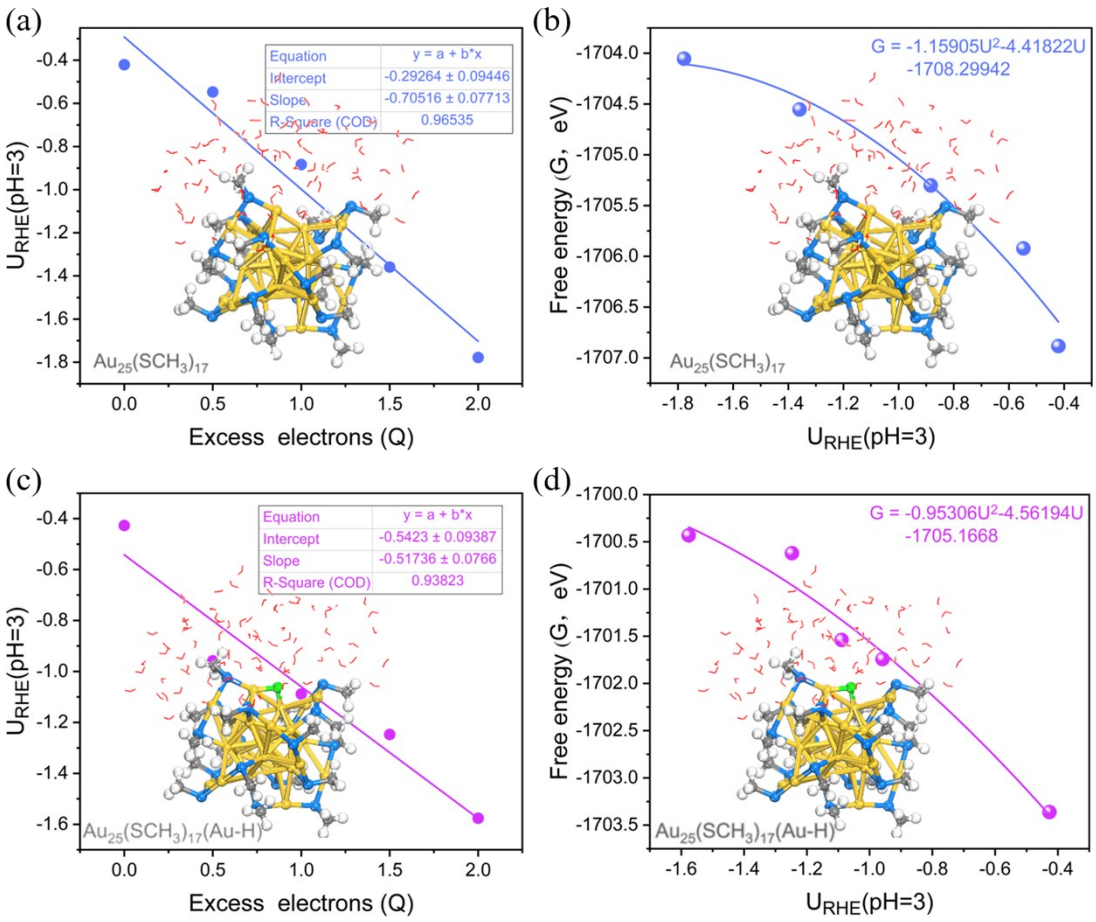

Figure S17. (a, c) The relationships between the excess electrons (Q) and the corresponded electrode potential U_{RHE} in pH = 3 on dethiolated $Au_{25}(SCH_3)_{17}$ and the H* system at Au-Au bridge sites. (b, d) Calculated free energies (points) and polynomial fits (lines) of dethiolated $Au_{25}(SCH_3)_{17}$ and the H* system at Au-Au bridge sites as a function of potential U_{RHE} in pH = 3, calculated using the constant potential method (cpm). The corresponding geometric snapshots optimized using an excess electron of 2e can also be seen in the inset where the adsorbed H is highlighted in green.

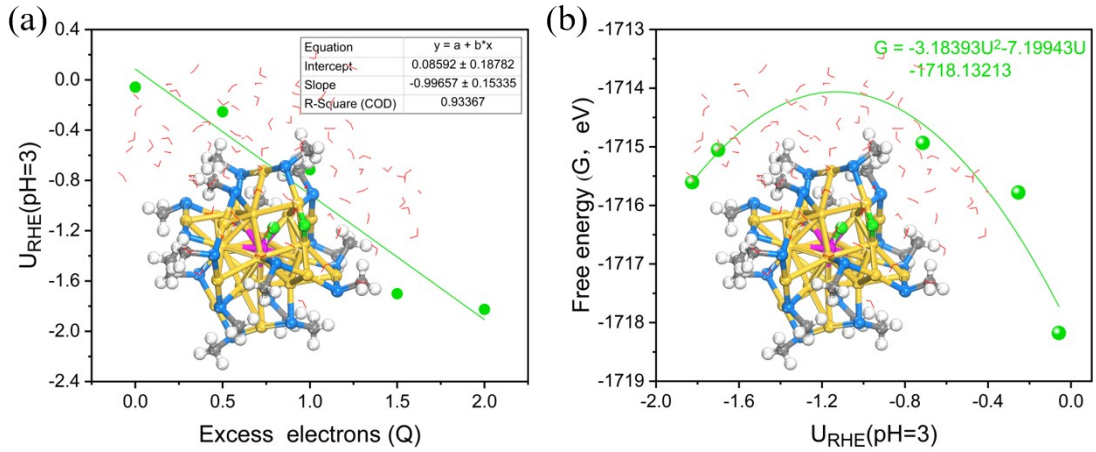

Figure S18. (a) The relationships between the excess electrons (Q) and the corresponded electrode potential U_{RHE} in pH = 3 on dethiolated $PtAu_{25}(SCH_3)_{17}$ with adsorption of two H. (b) And the calculated free energies (points) and polynomial fits (lines) as a function of potential U_{RHE} in pH = 3, calculated using the constant potential method (cpm). The corresponding geometric snapshots optimized using an excess electron of 2e can also be seen in the inset where the adsorbed H is highlighted in green.

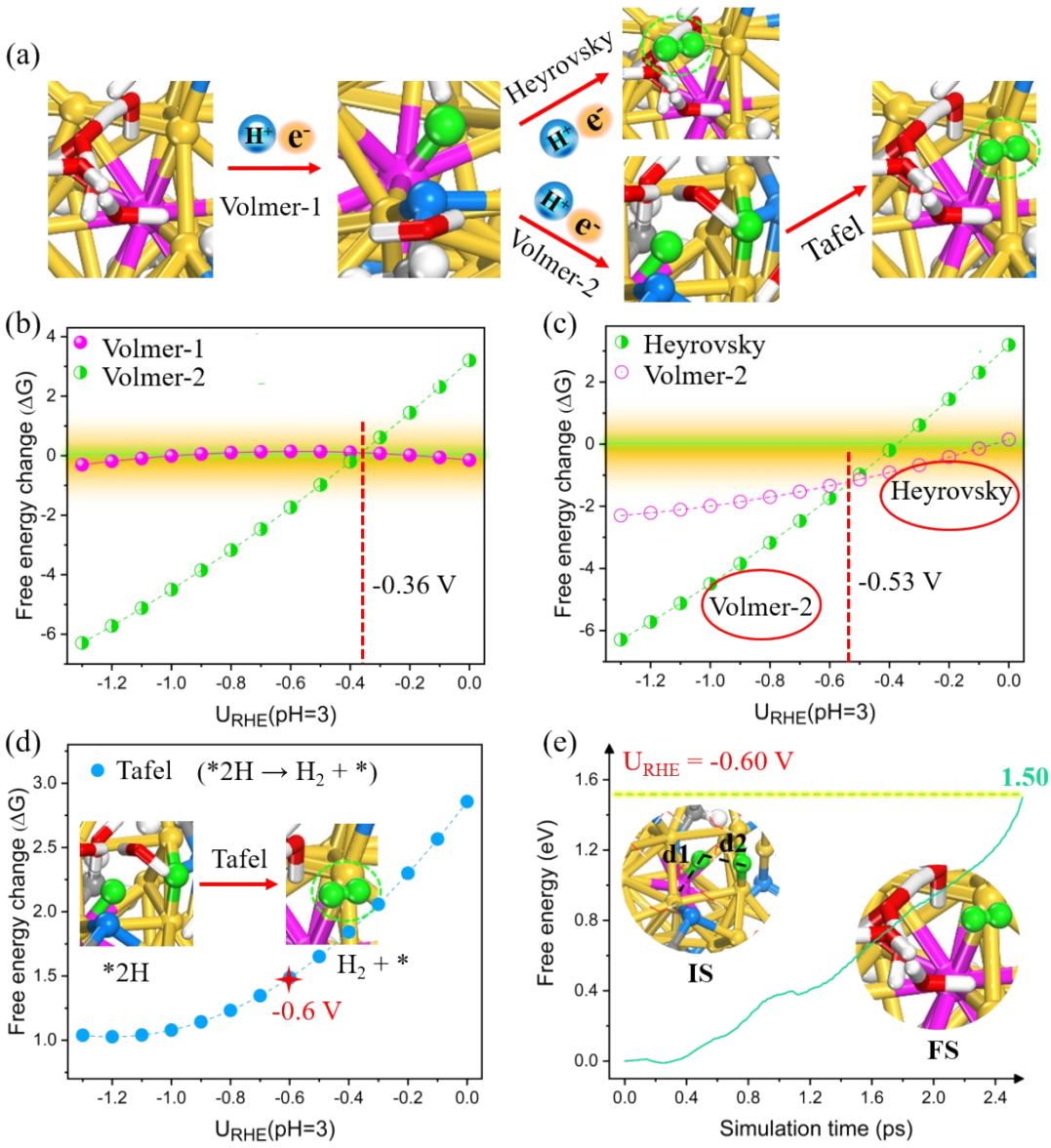

Figure S19. (a) The schematic of possible HER mechanism in dethiolated $PtAu_{25}(SCH_3)_{17}$. (b-d) Free energy changes of each elementary reaction as a function of electrode potential U_{RHE} in pH = 3. (e) Free energy profile of the formation of H_2 molecule during the slow-growth simulation at U_{RHE} = -0.60 V. The structures concerning the initial state and final state are denoted as IS and FS, respectively.

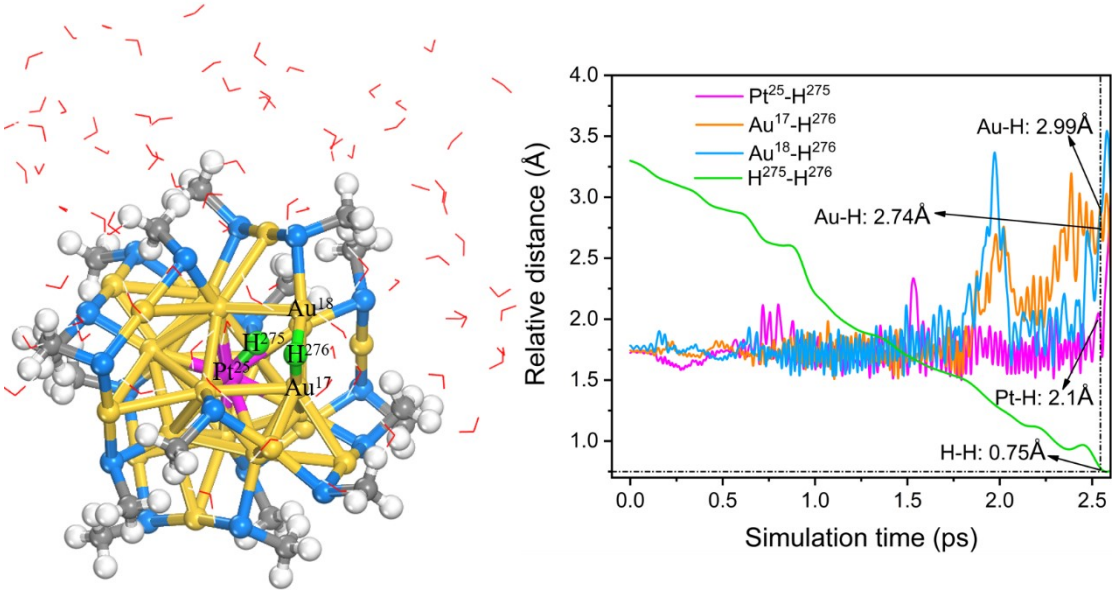

Figure S20. Dynamic evolution of bond length of Pt−H and Au−H for the H_2 formation via the Tafel process in dethiolated $PtAu_{25}(SCH_3)_{17}$ at U_{RHE} = -0.60 V, simulated by the slow-growth approach.

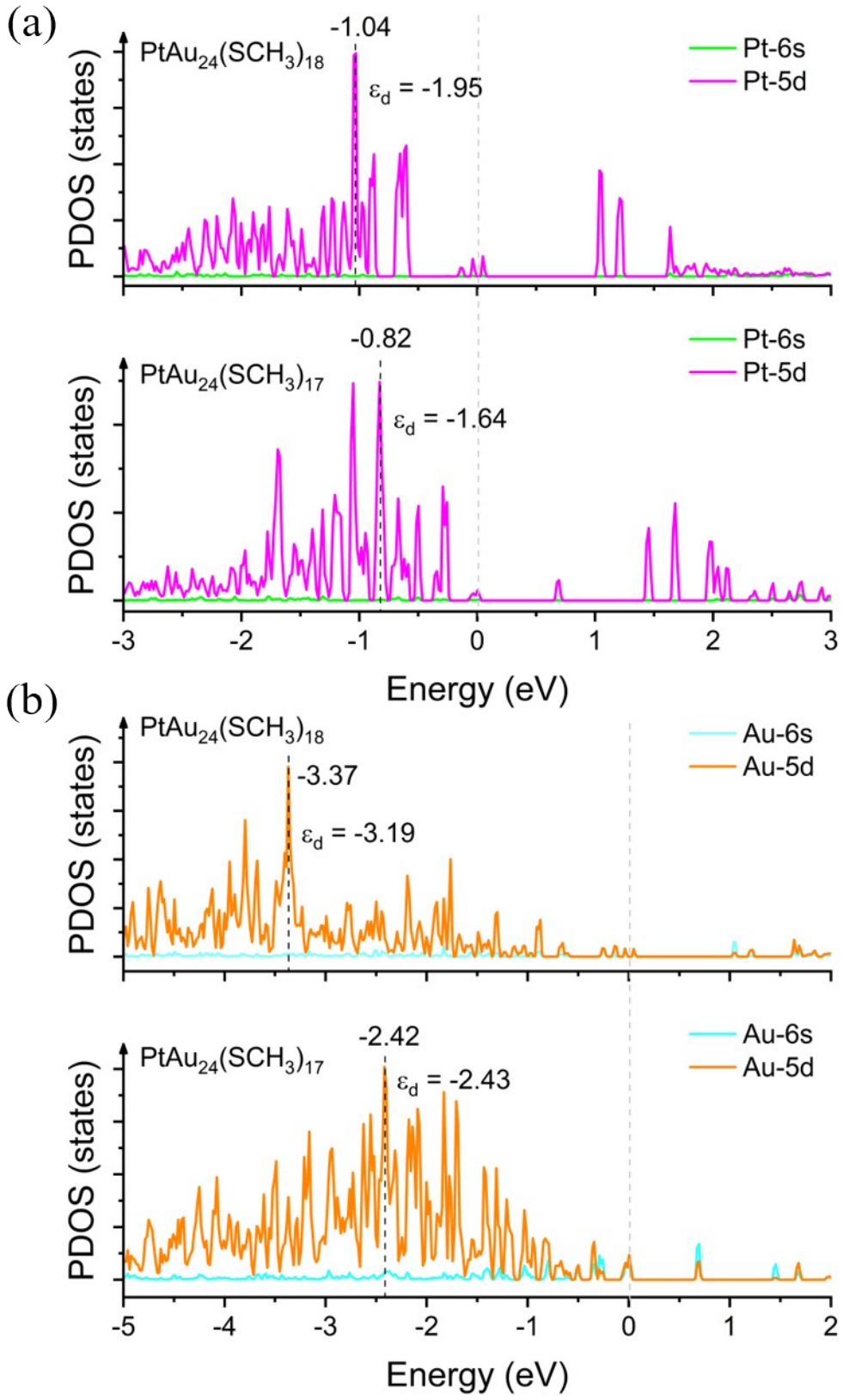

Figure S21. PDOS of the s-states and d-states of the active Pt (a) and Au-Au atoms (b) in the intact $PtAu_{24}(SCH_3)_{18}$ and dethiolated $PtAu_{24}(SCH_3)_{17}$ NCs.

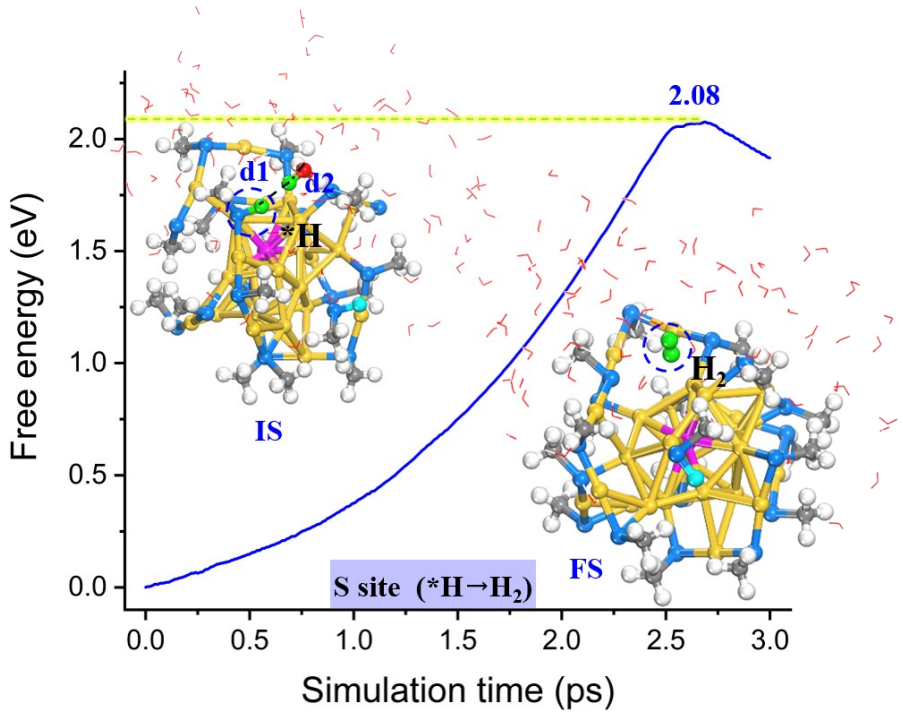

Figure S22. Free energy profiles of Heyrovsky reaction ($H^* + H_3O^+ + e^- = H_2 + * + H_2O$) on S sites during the slow-growth simulation at U_{RHE} = -0.1 V. The structures concerning the initial and final states are denoted as IS and FS, respectively.

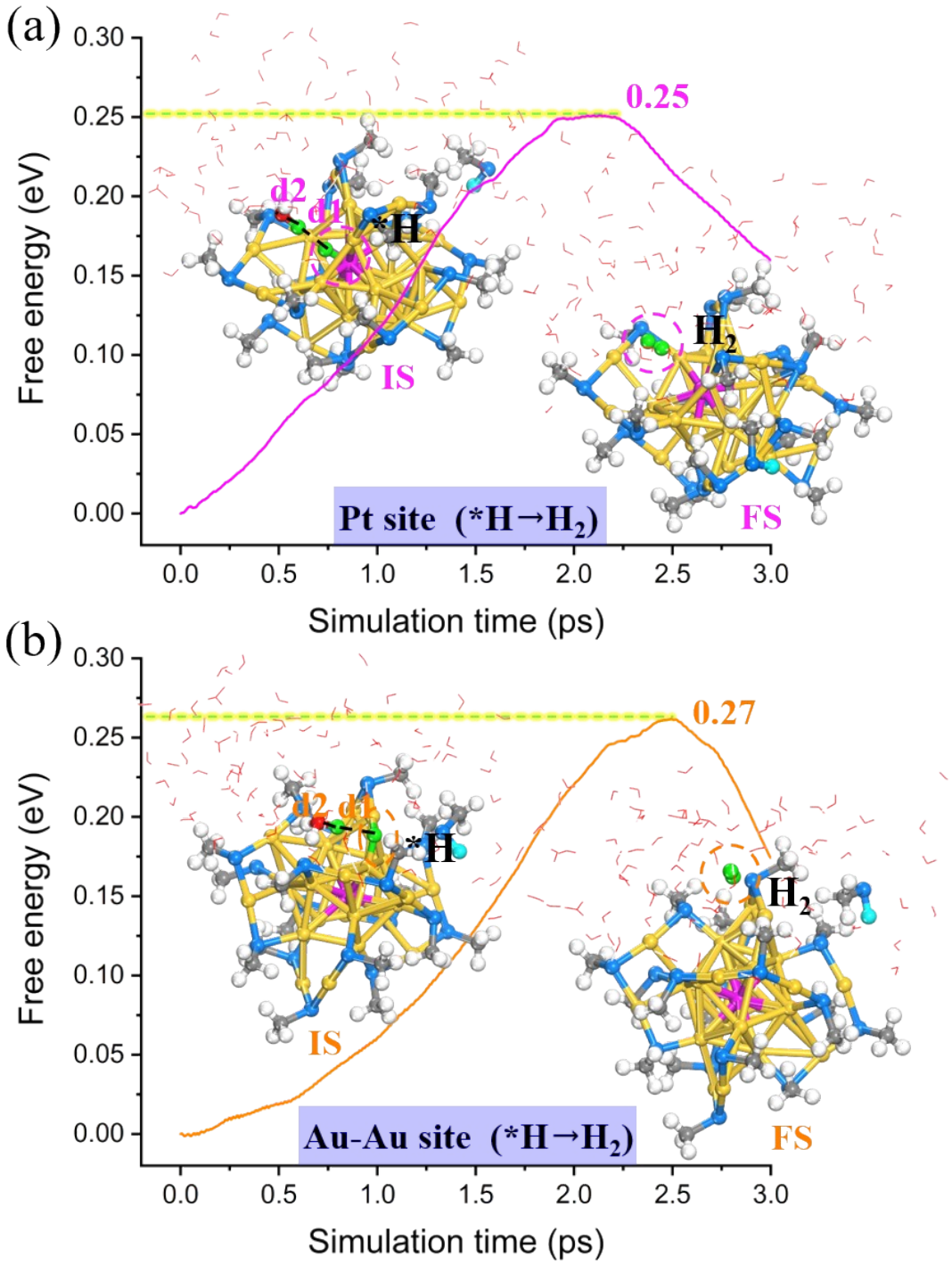

Figure S23. Free energy profiles of Heyrovsky reaction ($H^* + H_3O^+ + e^- = H_2 + * + H_2O$) on Pt (a) and dethiolated Au-Au (b) sites during the slow-growth simulation at U_{RHE} = -0.1 V. The structures concerning the initial and final states are denoted as IS and FS, respectively.

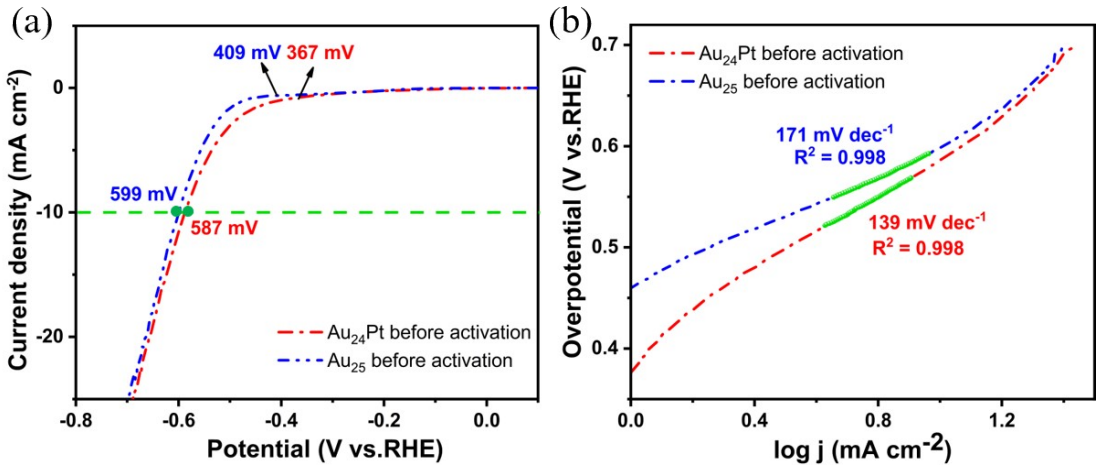

Figure S24. LSV curves (a) and Tafel plots (b) of $Au_{24}Pt$ and Au_{25} before activation.

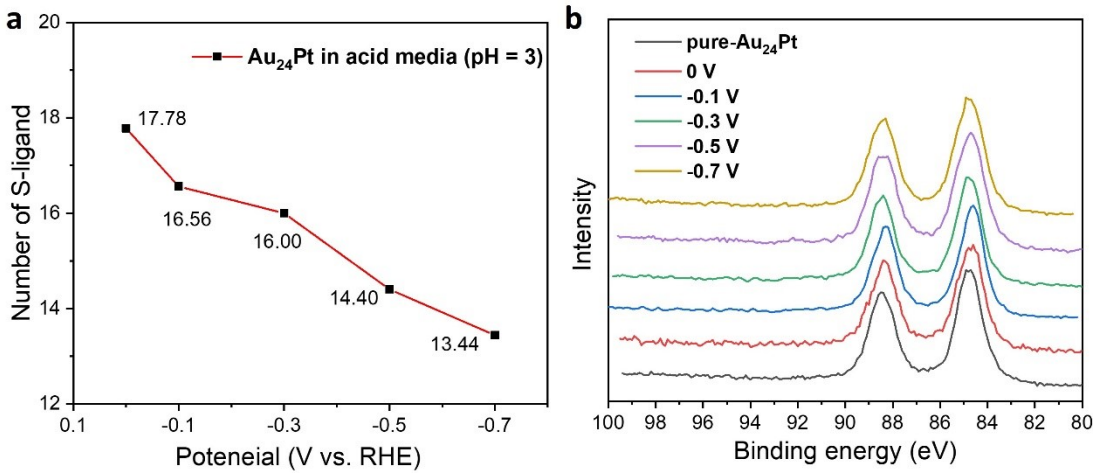

Figure S25. Remaining number of ligands in the $Au_{24}Pt$ cluster (a) and the XPS spectra for Au 4f (b) after 1 h electrochemical activation at different potentials in acid media (pH = 3).

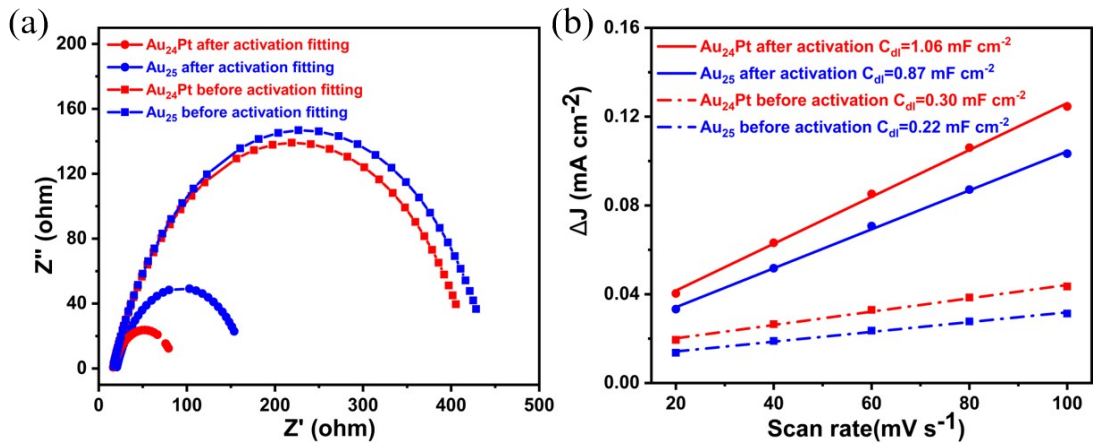

Figure S26. The electrochemical impedance spectrum of Au_{25} and $Au_{24}Pt$ in the 0.5 M Na_2SO_4 (pH = 3) (a) and the plots of current density as a function of scan rate derived from cyclic voltammograms of Au_{25} and $Au_{24}Pt$ (b).

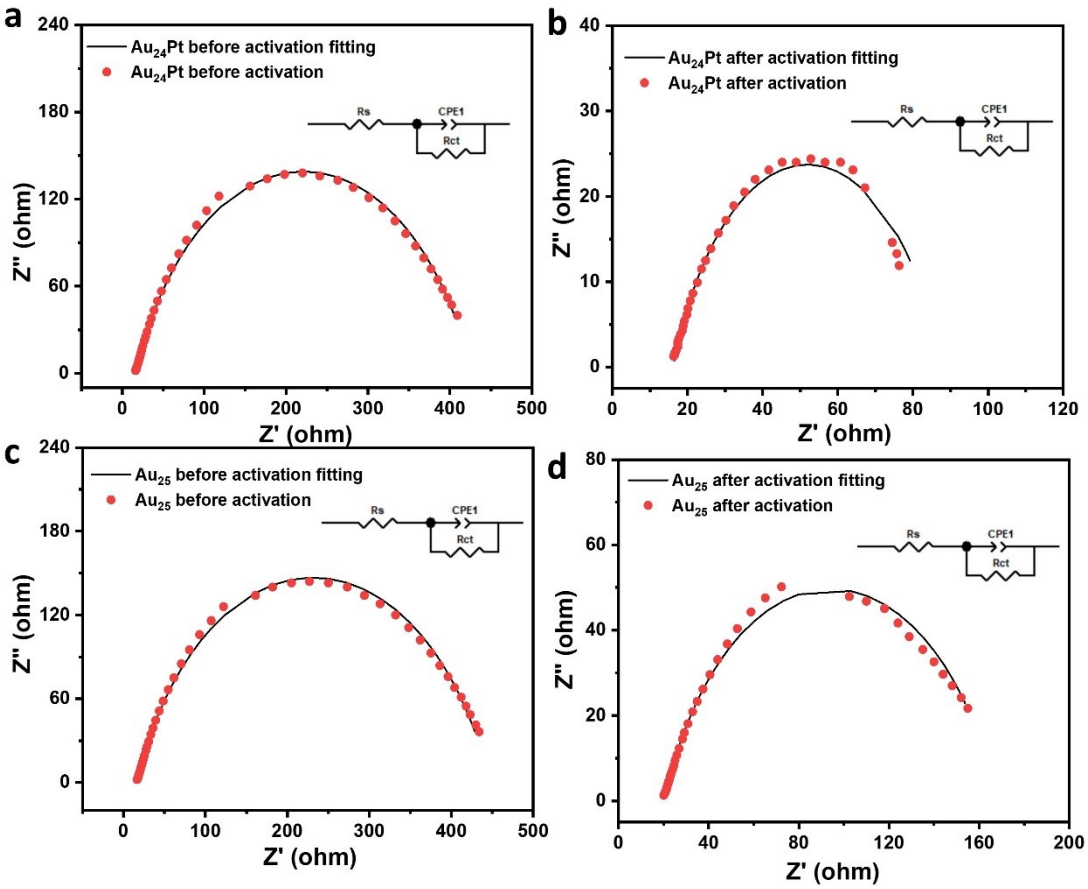

Figure S27. Electrochemical impedance spectra for $Au_{24}Pt$ (before (a) and after (b) activation) and Au_{25} (before (c) and after (d) activation) (Inset: equivalent circuit diagram).

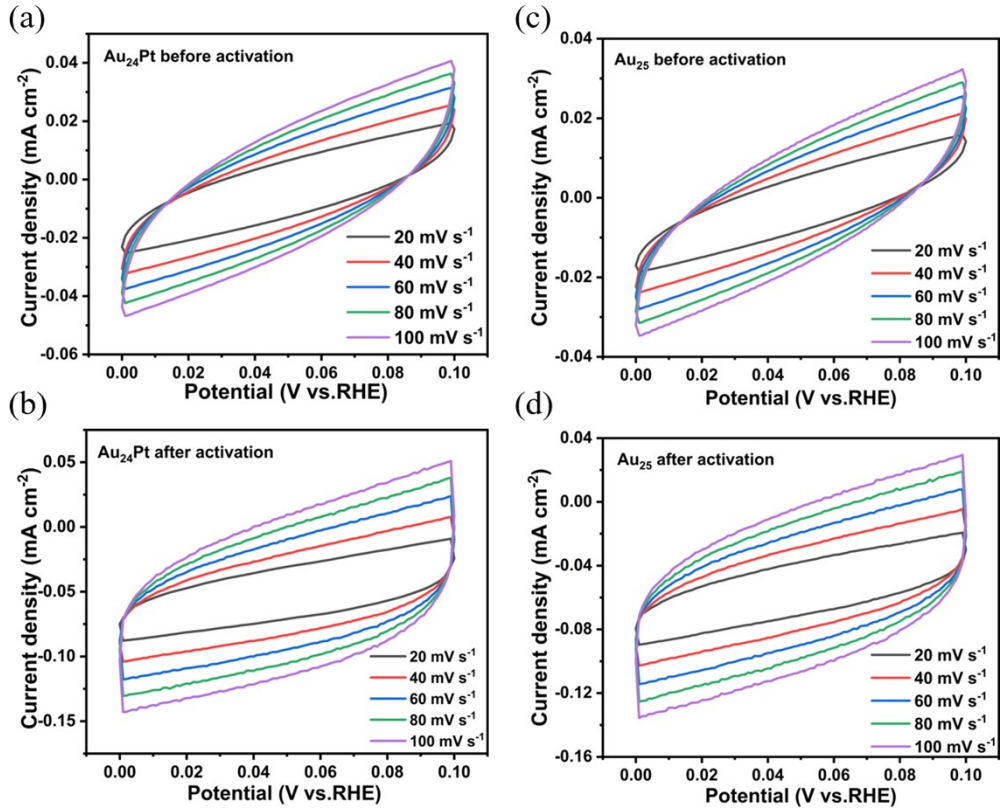

Figure S28. Cyclic voltammograms of $Au_{24}Pt$ before (a) and after activation (b), Au_{25} before (c) and after activation (d) at the region of 0 - 0.1 V in 0.5 M Na_2SO_4 (pH=3) at various scan rates.

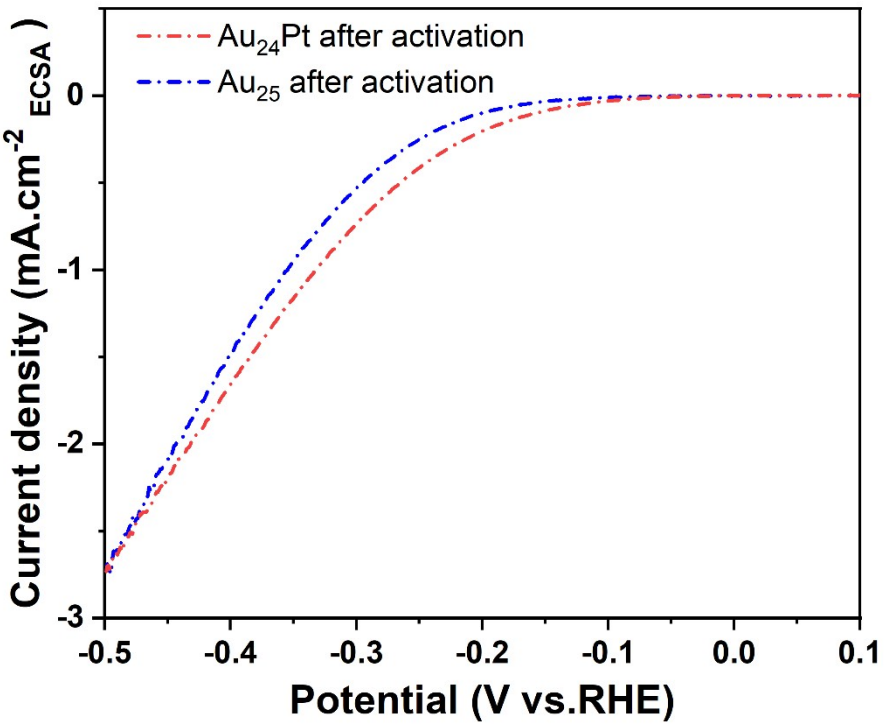

Figure S29. ECSA normalized HER polarization curves of Au_{25} and $Au_{24}Pt$ after activation.

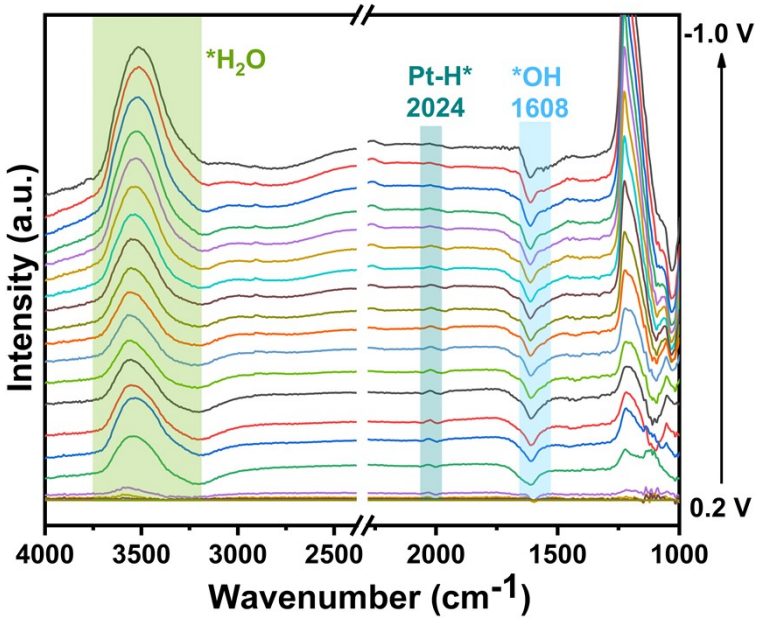

Figure S30. The electrochemical *in situ* FTIR (ATR-SEIRAS) potential-dependent spectra on the Pt/C electrode in 0.5 M Na_2SO_4 (pH=3).

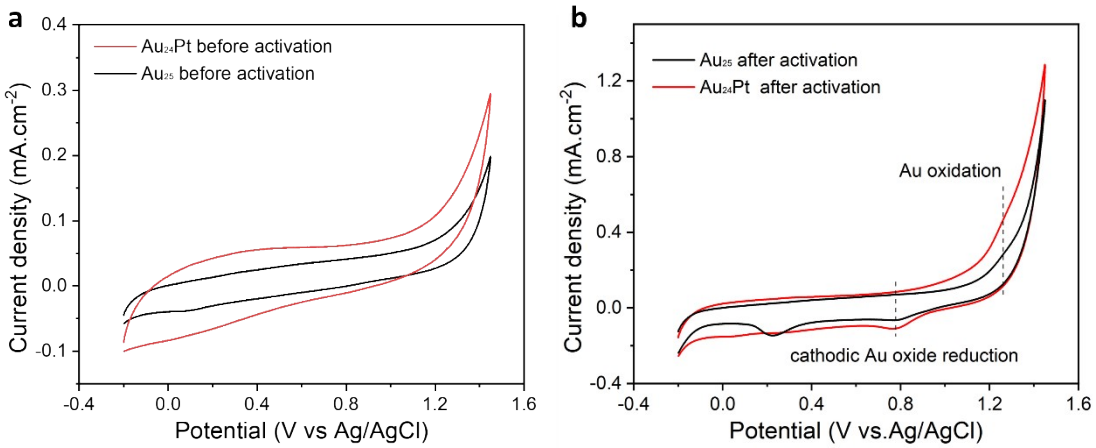

Figure S31. Cyclic voltametric (20 mV s^{-1}) studies for Au_{25} and $Au_{24}Pt$ before (a) and after (b) activation at the potential window from -0.2 V to 1.45 V vs. Ag/AgCl in 0.5 M Na_2SO_4 (pH = 3).

Table S1. Fitting results obtained from the EIS data for the HER in 0.5 M Na_2SO_4 (pH = 3)

Catalyst	Rct (Ω)	Rs (Ω)	CPE_1-T (mF)	CPE_1-P
$Au_{24}Pt$ (before activation)	411.2	16.11	0.0334	0.75873
$Au_{24}Pt$ (after activation)	74.19	16.15	0.06360	0.74705
Au_{25} (before activation)	432.1	16.46	0.03183	0.76185
Au_{25} (after activation)	148.1	15.17	0.05103	0.75477

References

1. G. Kresse and J. Furthmuller, Efficient iterative schemes for ab initio total-energy calculations using a plane-wave basis set, *Phys. Rev. B*, 1996, **54**, 11169-11186.
2. P. E. Blochl, Projector Augmented-Wave Method, *Phys. Rev. B*, 1994, **50**, 17953-17979.
3. J. P. Perdew, K. Burke and M. Ernzerhof, Generalized gradient approximation made simple, *Phys. Rev. Lett.*, 1996, **77**, 3865-3868.
4. I. L. Garzon and A. PosadaAmarillas, Structural and vibrational analysis of amorphous Au_{55} clusters *Phys. Rev. B*, 1996, **54**, 11796-11802.
5. W. Tang, E. Sanville and G. Henkelman, A grid-based Bader analysis algorithm without lattice bias, *J. Phys. Condens. Matter*, 2009, **21**, 084204.
6. T. Cheng, L. Wang, B. V. Merinov and W. A. Goddard, III, Explanation of Dramatic pH-Dependence of Hydrogen Binding on Noble Metal Electrode: Greatly Weakened Water Adsorption at High pH, *J. Am. Chem. Soc.*, 2018, **140**, 7787-7790.
7. T. Cheng, H. Xiao and W. A. Goddard, III, Reaction Mechanisms for the Electrochemical Reduction of CO_2 to CO and Formate on the Cu(100) Surface at 298 K from Quantum Mechanics Free Energy Calculations with Explicit Water, *J. Am. Chem. Soc.*, 2016, **138**, 13802-13805.
8. K. Xie, F. Wang, F. Wei, J. Zhao and S. Lin, Revealing the Origin of Nitrogen Electroreduction Activity of Molybdenum Disulfide Supported Iron Atoms, *J. Phys. Chem. C*, 2022, **126**, 5180-5188.
9. H. Reiss and A. Heller, The absolute potential of the standard hydrogen electrode: a new estimate, *J. Phys. Chem.*, 1985, **89**, 4207-4213.
10. F. Sun, F. Li and Q. Tang, Spin State as a Participator for Demetalation Durability and Activity of Fe-N-C Electrocatalysts, *J. Phys. Chem. C*, 2022, **126**, 13168-13181.
11. H. S. Pillai and H. Xin, New Insights into Electrochemical Ammonia Oxidation on Pt(100) from First Principles, *Ind. Eng. Chem. Res.*, 2019, **58**, 10819-10828.
12. Z. Duan and G. Henkelman, Surface Charge and Electrostatic Spin Crossover Effects in CoN_4 Electrocatalysts, *ACS Catal.*, 2020, **10**, 12148-12155.
13. D. Kim, J. Shi and Y. Liu, Substantial Impact of Charge on Electrochemical Reactions of Two-Dimensional Materials, *J. Am. Chem. Soc.*, 2018, **140**, 9127-9131.
14. N. Shuichi, A Unified Formulation of the Constant Temperature Molecular Dynamics Methods, *J. Chem. Phys.*, 1984, **81**, 511-519.
15. N. Shuichi, Constant Temperature Molecular Dynamics Methods, *Prog. Theor. Phys. Suppl.*, 1991, **103**, 1-46.
16. D. M. Bylander and L. Kleinman, Energy fluctuations induced by the Nosé thermostat, *Phys. Rev. B*, 1992, **46**, 13756-13761.
17. G. J. Martyna, M. L. Klein and M. Tuckerman, Nosé-Hoover chains: The canonical ensemble via continuous dynamics, *J. Chem. Phys.*, 1992, **97**, 2635-2643.
18. W. G. Hoover, Canonical dynamics: Equilibrium phase-space distributions, *Phys.*

Rev. A, 1985, **31**, 1695-1697.
19. T. K. Woo, P. M. Margl, P. E. Blöchl and T. Ziegler, A Combined Car−Parrinello QM/MM Implementation for ab Initio Molecular Dynamics Simulations of Extended Systems: Application to Transition Metal Catalysis, *J. Phys. Chem. B*, 1997, **101**, 7877-7880.
20. S. Takano, S. Ito and T. Tsukuda, Efficient and Selective Conversion of Phosphine-Protected $(MAu_8)^{2+}$ (M = Pd, Pt) Superatoms to Thiolate-Protected (MAu12)6+ or Alkynyl-Protected $(MAu_{12})^{4+}$ Superatoms via Hydride Doping, *J. Am. Chem. Soc.*, 2019, **141**, 15994-16002.